Grant Agreement No: 101096307

Full Title:	THz Industrial Mesh Networks in Smart Sensing and Propagation Environments
Start date:	01/01/2023
End date:	31/12/2025
Duration:	36 Months

Deliverable D3.1

Initial channel measurements in industrial environments at sub-THz frequencies

Document Type	Deliverable
Title	D3.1 Initial channel measurements in industrial environments as sub-THz frequencies
Contractual due date	31/10/2023 (M10)
Actual submission date	02/11/2023
Nature	Report
Dissemination Level	PUB
Lead Beneficiary	TUBS
Responsible Author	Varvara Elesina (TUBS)
Contributions from	Mate Boban, Tommaso Zugno (HWDU), Per Hjalmar Lehne (TNOR), Carla Reinhardt (TUBS)

Revision history

Version	Issue Date	Changes	Contributor(s)
V0.1	09/08/2023	Initial structure and assignment per partner	Varvara Elesina (TUBS), Carla Reinhardt (TUBS)
V0.2	20/09/2023	Input to section 2, 4 and 5	Mate Boban (HWDU), Tommaso Zugno (HWDU), Carla Reinhardt (TUBS), Varvara Elesina (TUBS)
V0.3	30/09/2023	Input to section 1, 2, 6, and 7	Per Hjalmar Lehne (TNOR), Varvara Elesina (TUBS)
V0.4	02/10/2023	Formation of the report	Varvara Elesina (TUBS)
V0.5	06/10/2023	Finalization of the report	Mate Boban (HWDU), Varvara Elesina (TUBS),
V0.6	20/10/2023	Review of the report	Víctor Torres (ANT, reviewer) Davy Gaillot (CNRS, reviewer)
V0.7	23/10/2023	Preparing version for submission	Mate Boban (HWDU), Varvara Elesina (TUBS), Carla Reinhardt (TUBS)
V1.0	02/11/2023	Final Review and acceptance	Danila Ferretti (CNIT) Luca Sanguinetti (CNIT) Thomas Kürner (TUBS)
V1.2	15/11/2024	Rejection letter addressing	Varvara Elesina (TUBS), Mate Boban (HWDU)
V1.2	20/12/2024	Final editing	Flaminia Saratti (CNIT)
V2.0	20/12/2024	Approved version	Luca Sanguinetti (CNIT)

Disclaimer

The content of the publication herein is the sole responsibility of the publishers, and it does not necessarily represent the views expressed by the European Commission or its services.

While the information contained in the documents is believed to be accurate, the authors(s) or any other participant in the TIMES consortium make no warranty of any kind with regard to this material including, but not limited to the implied warranties of merchantability and fitness for a particular purpose.

Neither the TIMES Consortium nor any of its members, their officers, employees or agents shall be responsible or liable in negligence or otherwise howsoever in respect of any inaccuracy or omission herein.

Without derogating from the generality of the foregoing neither the TIMES Consortium nor any of its members, their officers, employees or agents shall be liable for any direct or indirect or consequential loss or damage caused by or arising from any information, advice, inaccuracy, or omission herein.

Copyright message

© TIMES Consortium, 2022-2025. This deliverable contains original unpublished work except where clearly indicated otherwise. Acknowledgement of previously published material and of the work of others has been made through appropriate citation, quotation, or both. Reproduction is authorised provided the source is acknowledged.

Table of Contents

List of Abbreviations

AoA	Angle of Arrival
AoD	Angle of Departure
AP	Access Point
AS	Angular Spread
B2B	Back-to-Back
CIR	Channel Impulse Response
DS	Delay Spread
EMF	Electromagnetic Field
ISAC	Integrated Sensing and Communications
KF	K-Factor
LOS	Line-of-Sight
LSP	Large-scale Parameters
M2M	Machine-to-Machine
MPC	Multipath Component
NLOS	Non-Line-of-Sight
OLOS	Obstructed-Line-of-Sight
OTA	Over the Air
PDP	Power Delay Profile
PG	Path Gain
PL	Pathloss
RT	Real Time
Rx	Receiver
THz	Terahertz
Tbps	Terabits per second
Tx	Transmitter
UE	User Equipment

Executive Summary

TIMES project's ultimate goal is to create a sophisticated THz-based smart radio ecosystem, that work in complex scenarios involving many different devices. This ecosystem should be able to provide wired-level performance in various aspects such as data rates reaching terabits per second (Tbps), extremely low latency, advanced detection capabilities and exceptional reliability. To achieve this long-term goal, it is proposed to use the following three pillars:

- Exploiting ultra-wide bandwidth and sensing-friendly characteristics of THz communications.
- Deploying intelligent mesh networks in smart propagation environments.
- Enabling high-definition integrated sensing and communications (ISAC).

The first pillar involves the investigation of radio communication systems and the development of channel models, that are impossible without channel measurements. Within the TIMES project, it is planned to carry out three main types of measurements:

- Measurements in static environments
- Measurements in time-variant scenarios
- Measurements to characterize developed components.

The first and second types of measurements will be carried out at an early stage of the project, during the implementation of Task 3.1. The results of this will be presented in this deliverable.

1. Introduction

THz frequencies are expected to be crucial in the development of wireless communication in industrial applications due to offering possibilities for targeting Tbps data rates, achieving high level of reliability, high precision localization and imaging accuracy, and decreasing latency. Development and implementation of wireless communication technologies are not realizable without comprehensive channel models. While creating channel models requires a foundation of measurement data. In this context, the aim of WP3 in the TIMES project is to conduct channel measurements and base on it create channel models for industrial environment, relevant at 300 GHz.

The purpose of this activity is to perform channel measurements at 300 GHz based on scenarios identified in Deliverable 2.1. These measurements include both inter- and intra-device scenarios as well as time-variant and time-invariant cases. Time-variant scenarios include two variations: 1) static transmitter and receiver and moving obstacles; 2) static transmitter and moving receiver. In addition to the required scenarios list, characterization of pathloss and large-scale parameters were conducted for different visibility cases in industrial workshop environment. Measurements were conducted by TIMES project partners: HWDU and TUBS separately, providing an opportunity to compare results and obtain a more diverse database of measurement data. This diversity will undoubtedly enhance the quality of future models. The measurements were conducted in three different industrial workspaces with varying machine densities. All obtained measurement data was evaluated and presented as plots and parameters tables, which can be used for further channel modelling. The frequency range descriptions of "Sub-THz" (0.1 – 1 THz) and "THz" (0.1 – 30 THz) overlap, and the 300 GHz frequency used in the measurements described in this document falls within both descriptions. Consequently, for the purposes of this deliverable, these terms are interchangeable and are both utilized.

1.1. Scope

This deliverable describes radio channel measurements conducted at 300 GHz in industrial environments, covering all the specified scenarios outlined in Deliverable 2.1. It includes equipment parameters, setups details and analysis of measured data. Also, it provides a brief introduction to aspects of EMF exposure at THz frequencies.

1.2. Audience

The audience for this deliverable is assumed to be TIMES project partners, working in the fields of channel model creation.

1.3. Structure

The rest of the document is structured as follows:

- Section 2 presents the literature review of publication dedicated to channel measurements at 300 GHz in industrial environments.
- Section 3 provides a brief overview of the measurement equipment used by HWDU and TUBS for the TIMES project channel measurements.
- Section 4 describes industrial workspaces where channel measurement for the TIMES project were conducted.
- Section 5 presents the scenario descriptions for the channel measurements and evaluation results.
- Section 6 gives a brief introduction to aspects of EMF exposure at THz frequencies.
- Section 7 concludes the deliverable with key findings.

2. Literature review of previous channel measurements in industrial environments in THz frequencies

Before starting measurements, literature research was conducted. Only two publications were found dealing with measurements at 300 GHz and in industrial environments.

[1] presents angle-resolved measurements in an industrial environment with a carrier frequency of 300 GHz. Measurements consisted of three different scenarios conducted in various workspaces. The first scenario was performed in the storage and prototyping area of the production hall and included 10 measurement points. Tx was placed at 2.7m high with varying alignment, and receiver height was 1.5m with fixed orientation. The second scenario took place on the shop floor of the production hall, which was densely packed with machinery and robots. Tx height was 2.7m and it was located in the centre of the workspace, its antenna aimed at the measurement points. Rx height was 1.5m and it was placed at four positions: two LOS and two NLOS. The last scenario took place in a narrow hallway with metallic plates in the walls: flat on one side and perforated on the other side. Tx and Rx heights were 1.5m. Tx was positioned outside the hallway, Rx inside. There were four scenarios in total: two with Tx near the hallway opening and facing to Rx and two with Tx on the opposite side of perforated wall.
In all scenarios, measurements were taken with 24 approached angles around each measurement point, spaced in 15° steps covering a full 360° in the azimuth plane. After measurement evaluation omni-directional instantaneous PDPs were obtained and used to estimate channel parameters such as Path Gain (PG), Pathloss (PL), Delay Spread (DS) and Angular Spread (AS).
The following conclusions and observations were made by the paper's authors:

1) For LOS and OLOS measurements, the strongest path is the LOS. For NLOS, the strongest MPCs direction can be determined.
2) For LOS cases, approximately 70% of the total accumulated power is in the first strongest path.
3) DS and AS values behave consistently. When DS values increase or decrease, AS exhibits a corresponding behaviour.
4) An average Pathloss (PL) in storage and prototyping area was 101.6 dB; for the production shop floor scenario an average PL was 104.0 dB; in the metal hallway scenario average PL was 92.7 dB.

Publication [2] introduced double-polarized, double-directional measurements at 300 GHz. Measurements reconstructed scenario of transmission between an external access point (Tx) and user equipment (Rx) located inside a milling machine. Measurements consist of two setups. The first setup estimates glass penetration losses and window frame obstruction losses. Tx and Rx antennas were manually aligned as the window was opened in increments of 0.5 cm, moving from LOS through the glass to OLOS through the frame and finally to LOS in the free space. In the second setup Tx scans azimuth and across the machine and RX scans azimuth from -180° to 165° and elevation from -45° to 45°. Measurements were conducted with the machine window open and in the case when the frame covers LOS, as well as with the window obstructed by a forklift. Measurements were provided in both vertical and horizontal polarizations. Measurement results include: 1) polarimetric marginal power angular/delay profiles; 2) polarimetric synthetic omni-directional PDP; 3) polarimetric power azimuth/elevation profiles.
The following observations were made:

1) Besides LOS multiple reflections can be identified using propagation distance and different TX and RX scan directions. Most of the reflections come from the metal components of the machine (such as frames or positioning axes).
2) Even in case of obstruction (by frame or forklift), there are multipath components (MPCs) in the channel.

Based on the lack of publications in this area and on the results of the two papers presented above, several conclusions can be drawn. First, 300 GHz communications are possible in industrial environments. Secondly, further measurements are urgently needed. Third, further measurements should cover the comprehensive list of scenarios: from more detailed studies of LOS and NLOS cases to time-varying channel measurements, which is very important in the case of industrial applications.

3. Measurement equipment description

3.1. Huawei channel sounder

HWDU will perform channel measurements using a dual-polarized ultra-wideband channel sounder composed of a Tx unit, Rx unit, and a control unit. Tx and Rx units are mounted over positioners that can scan the angular domain in azimuth and elevation. The block diagram of the measurement system is depicted in Figure 1.

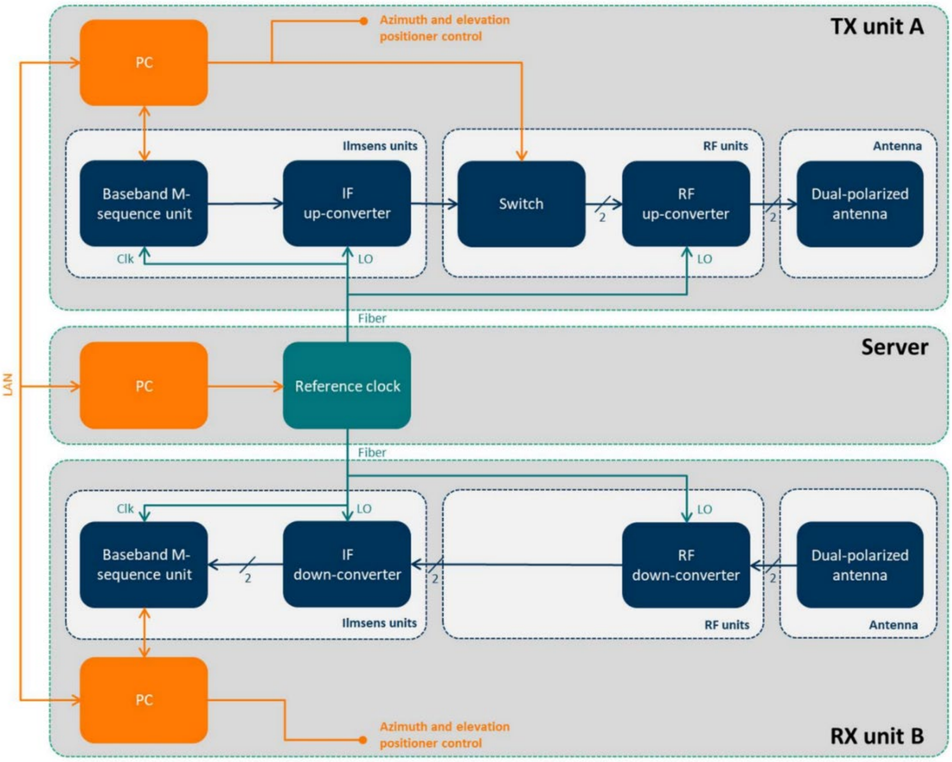

Figure 1 Overall structure of the HWDU channel sounder

Tx and Rx units are composed of three main components, namely Ilmsens modules, RF modules, and antennas. At the transmitter side, the Ilmsens module generates an excitation signal is a 12-bit maximum-length binary sequence (MLBS), also known as M-sequence with length 4095 samples. The baseband signal is then up converted using an integrated IF stage and used as input to the RF module. Finally, the RF module up-converts the IF signal to 300 GHz using internal multipliers (x48). On the receiving side, the RF signal is down converted to IF and used as input to the Ilmsens unit to obtain the baseband signal. The system supports different types of antennas, including highly-directive horn and open-ended waveguide antennas.

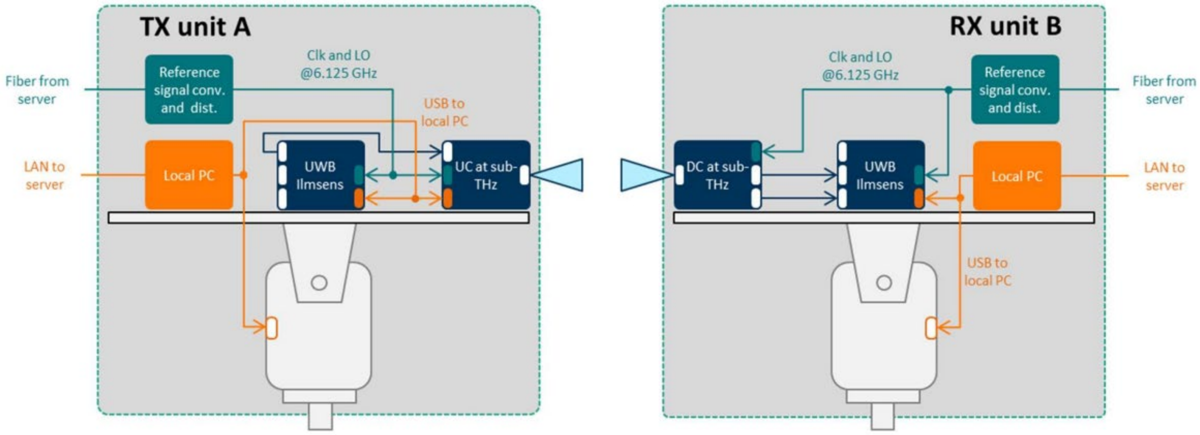

Figure 2 Schematic of the channel sounder and the positioners

The Channel Impulse Response (CIR) is obtained by cross correlating the received signal with a copy of the transmitter signal in the frequency domain. To characterize the omni-directional properties of the channel, angular domain is sampled by rotating directive antennas at the Tx and Rx in azimuth and elevation.

The details of the channel sounder are reported in Table 1 below.

Table 1 HWDU Channel Sounder parameters

Parameter	Value
TX power	-8 dBm
TX antenna gain	25 dBi
RX Antenna Gain	25 dBi
Received Power	-49.54 dBm
M-sequence order	12
Sequence length	4095
IF Frequency	6.2 GHz
Measurement bandwidth	6.2 GHz
Bandwidth (after calibration)	5 GHz

3.2. TUBS channel sounder

TUBS utilizes a correlative channel sounder (CS) to measure the CIR of a radio channel. For a comprehensive understanding of the measurement system, please refer to [3]. The measurement system's schematic view is presented in Figure 3, and detailed CS parameters are listed in Table 2.

In TIMES measurements will be conducted at a frequency of 300 GHz. Various measurement setups can be used, including:

- **Static channel measurements**, in which Tx and Rx are fixed in a chosen constellation.
- **Full-omni 360° rotational measurements,** where every combination of the Angle of Departure (AoD) and Angle of Arrival (AoA) between the antennas can be measured. These measurements provide information about the spatial properties of the environment.

- **Multiple antenna setups**, involving Multiple-Input Single-Output (MISO) (2x1), Single-Input Multiple Output (SIMO) (1x2) or Multiple-Input Multiple Output (MIMO) (2x2) configurations that can be measured.
- **Real-Time (RT) measurements** are used for dynamic scenarios and MIMO/MISO measurement setups. Due to the large amount of data generated from these type of measurements (approximately 576 MB per second), careful planning is required.
- **Averaged measurements.** This technique involves the averaging of multiple CIR and is especially useful in static scenarios because it improves the dynamic range by averaging.
- **For dynamic scenarios, a rail system can be used**. This system allows the installation of one or two Tx/Rx or objects, as shown in Figure 4.

Measurement limitations and constraints

- Due to the constraints of the measurement system, the maximum distance between Tx and Rx is 15m.
- For RT measurements, scenarios with a maximum duration of up to 10 seconds should be captured to allow enough time for subsequent post-processing.
- In dynamic scenarios, when Rx is in motion, it is important to minimize vibrations.

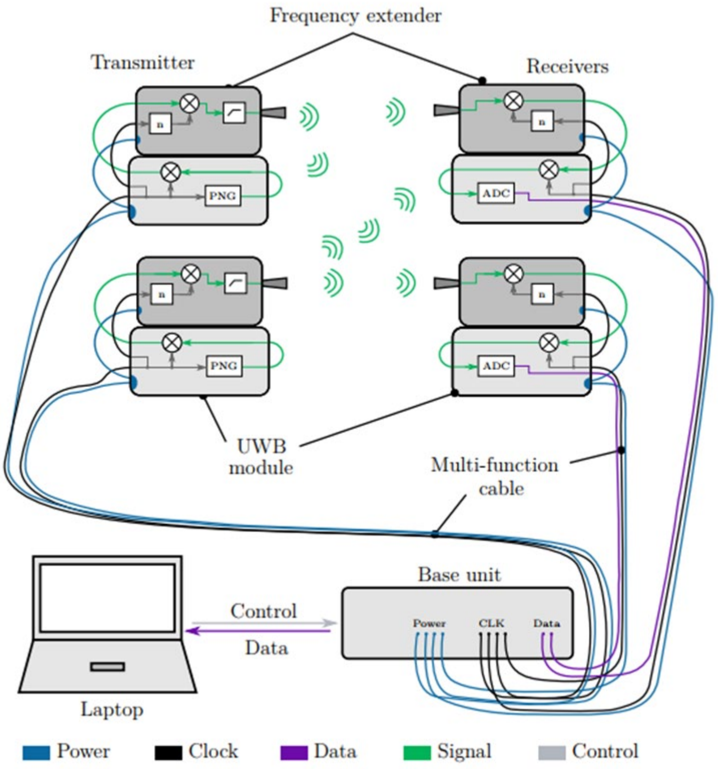

Figure 3 Schematic view of the TUBS CS

Table 2 TUBS Channel Sounder parameters

Parameter	Value
Clock Frequency	9.22 GHz
Bandwidth	approx. 8 GHz
Chip duration	108.5 ps
M-sequence order	12
Sequence length	4095
Sequence duration	444.14 ns
Subsampling factor	128
Acquisition time for one CIR	56.9 µs
Measurement Rate	17,590 CIR/s
Centre Frequencies	9.2/64.3/304.2 GHz
SISO/MIMO	Up to 2x2

Figure 4 Rail system used for dynamic measurement scenarios

4. Description of measurement environments

4.1. Industrial workshop

Measurements were performed in an industrial workshop depicted in Figure 5. The workshop comprises multiple tools, milling machine, a large industrial crane, chairs, tables, etc. Two measured scenarios are depicted in the Figure 5: 1) inter-device, where a transmitter/access point outside of a machine/device is communicating with a receiver/UE that is inside the machine (i.e., AP1 to UE communication); and 2) inter-device, where the transmitter/access point is also inside the machine (i.e., AP2 to UE communication). The third scenario is depicted in Figure 6, where a set of transmitter and receiver locations are dispersed across the same industrial workshop in order to characterize the characteristics of pathloss and large-scale parameters in the environment for both LOS and NLOS channels.

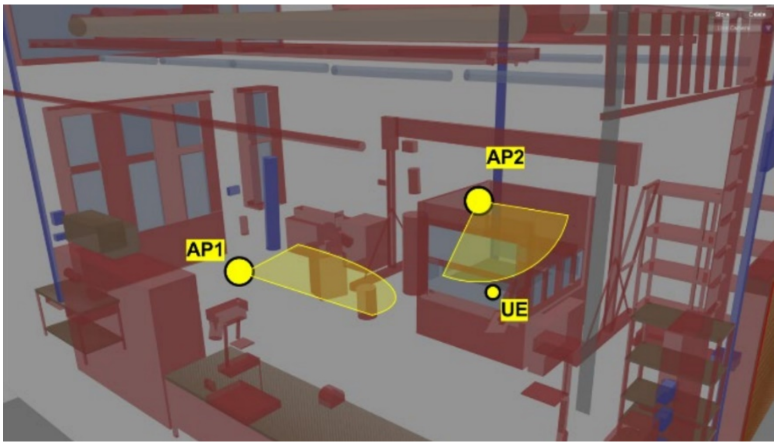

Figure 5 Industrial workshop environment

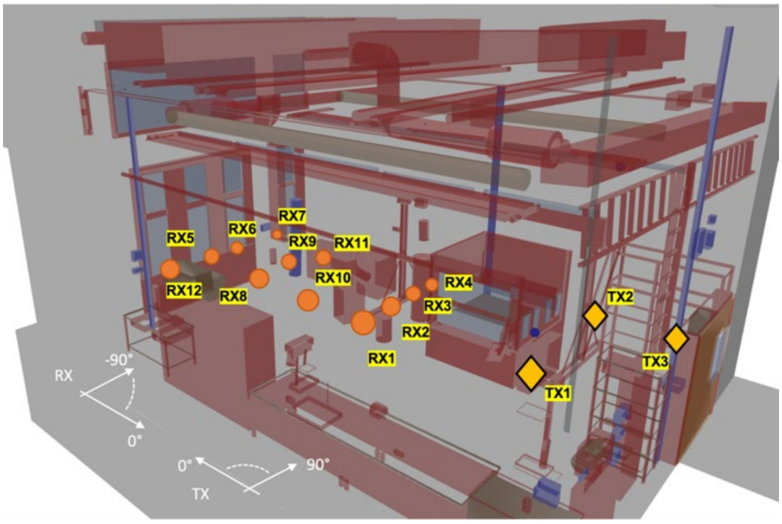

Figure 6 Schematic of the room and positions of the TX and RX.

4.2. Robotic laboratory

TUBS measurements were taken in two different workspaces. The first workspace is a robotic lab that houses a few different types of robotic manipulators, Figure 7. This laboratory belongs to the Institute for Robotics and Process Control, a part of the TU Braunschweig. In this document, we will refer to it as "robotic lab".

a

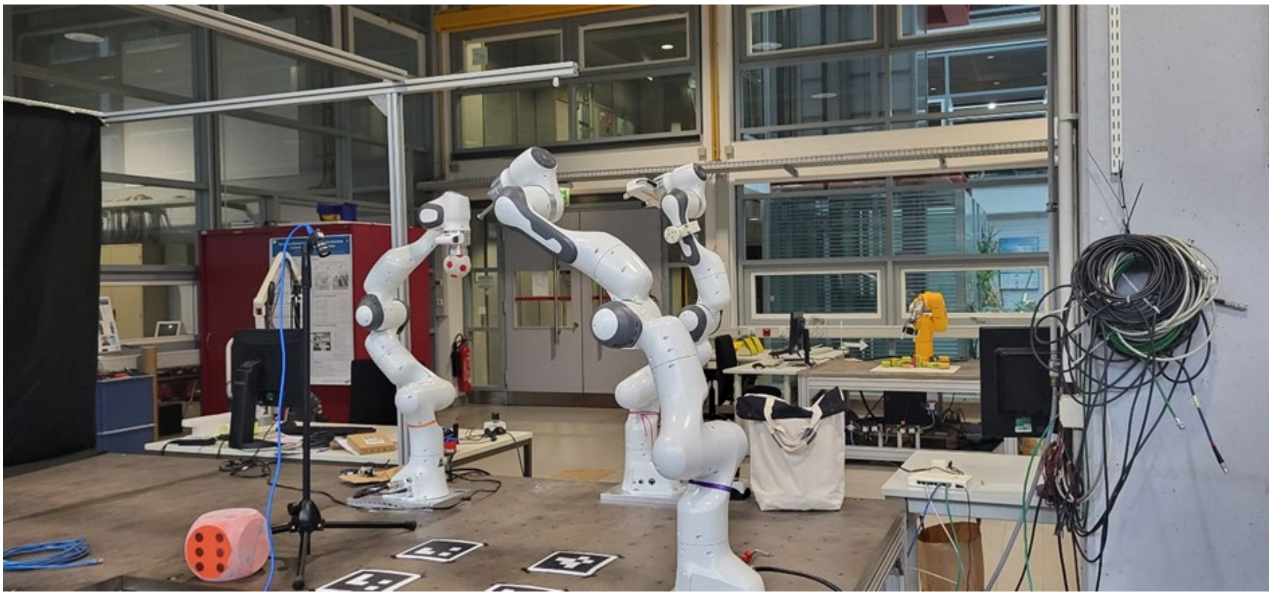

(b)

Figure 7 Robotic lab workspace view

4.3. Big industrial space

The second measurement workspace was a comprehensive industrial space with numbers of different machine types, metal surfaces, not ordinary ceiling and three different heights levels (Figure 8). This workspace belongs to the Institute of Machine Tools and Production Technology, which is a part of TU Braunschweig. For simplicity, we will refer to it as the 'big industrial workspace'.

Figure 8 Big industrial workspace view

5. Measurement scenarios and results

5.1. Characterization of pathloss and large-scale parameters in LOS and NLOS in industrial workshop environment

As depicted in Figure 6, the Tx and Rx were located at different locations at 1.72 m high in 3 and 12 different positions in the room, respectively. This choice is motivated to sample the channel in as many different possible locations and generate LOS and NLOS visibility conditions. However, not all the combinations of links were measured. In total, there are 10 LOS and 10 NLOS links, as indicated in the 3-Dimensional (3D) Tx-Rx distance coded in blue and red colours in Table 3, respectively. The angular reference is local and clockwise: 0° azimuth at Tx and at Rx is displayed in Figure 6.

Table 3 3D TX-RX distance of the different measured links and visibility, blue: LOS and red: NLOS.

	Rx1	**Rx2**	**Rx3**	**Rx4**	**Rx5**	**Rx6**	**Rx7**	**Rx8**	**Rx9**	**Rx10**	**Rx11**	**Rx12**
Tx1	2.99	3.03	3.13	3.30	6.49	6.51	6.65	5.74	5.76	4.99	6.19	
Tx2	4.01		3.77	3.74	7.39	7.31	7.24		6.57			
Tx3							8.24					9.27

5.1.1. Analysis of the measurement results

The dynamic range after calibration (maximum to minimum peaks of the synthetic omni-directional power delay profile after noise floor removal) for the different bands is displayed in Figure 9. A considerably lower dynamic range is observed in the THz measurements for NLOS, product of the limited TX power in the measurement system. This dynamic range is used later for a fair comparison of the measured large-scale parameters (LSPs) between the different bands.

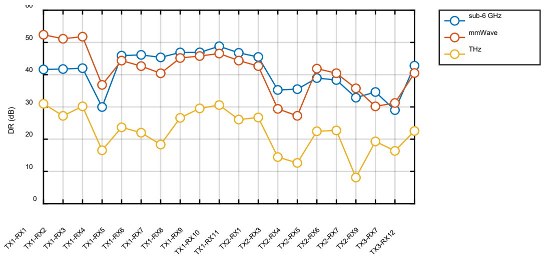

Figure 9 Dynamic range of the different links over the different bands

Two links were selected to compare in detail, the LOS TX1-RX1 link and the NLOS TX1-RX4 link, in which the RX is behind the CNC machine, as shown in Figure 6. The multi-band power bi-azimuth profile at TX and RX are displayed in Figure 10. In addition, the multi-band synthetic omni-directional PDP for these links are displayed in Figure 11. Multiple common clusters of MPCs can be observed in both links in the different bands. In the LOS case, there are three dominant scatterers within the 30 dB dynamic range: the LOS path, a reflection on the CNC machine, namely S1, at $(\varphi,\phi) = (30°, -30°)$, and on the wall, S2, $(\varphi,\phi) = (-60°, 60°)$.

On the other hand, in the NLOS case there are multiple dominant clusters within the same dynamic range. The first one is the diffracted component S1 at $(\varphi,\phi) = (30°, 30°)$. As seen in Figure 12 (b)Figure 2, the energy of this path decreases with increasing frequency, which is due to the decreased diffraction angle with increasing frequency. This in turn results in the diffracted path not being visible at THz within the selected dynamic range. Moreover, similarly to the LOS link TX1-RX1, a reflection on the wall S2 is captured at$(\varphi,\phi) = (-60°, 60°)(\varphi,\phi) = (-135°, 45°)$. Reflection in the machinery behind RX4 is observed$(\varphi,\phi) =$

$(15^\circ, 165^\circ)$ and labelled as S4. Higher order interactions are also identified, such as a double reflection in the cupboard and the frames of the door/window at the end of the room, labelled as S5, is observed $(\varphi, \phi) = (-30^\circ, 150^\circ)\,(\varphi, \phi) = (-30^\circ, 150^\circ)(\varphi, \phi) = (-150^\circ, 15^\circ)$.

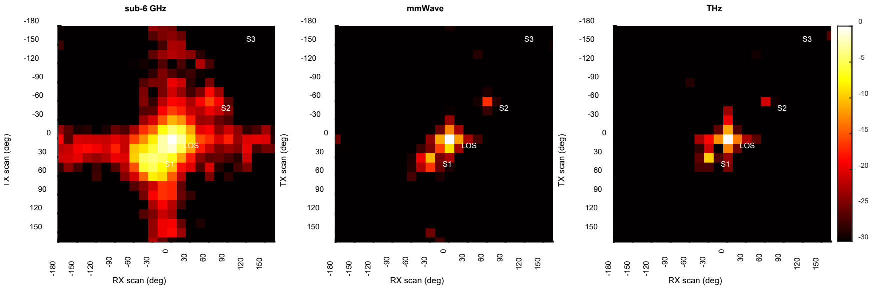

a. Multiband power bi-azimuth profile at TX and RX in the LOS link TX1 – RX1

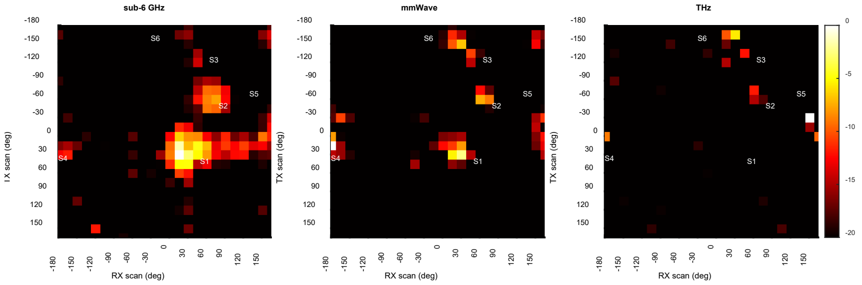

b. Multiband power bi-azimuth profile at TX and RX in the LOS link TX1 – RX4

Figure 10 Multiband power bi-azimuth profile at TX and RX in a (a) LOS link, and (b) NLOS link

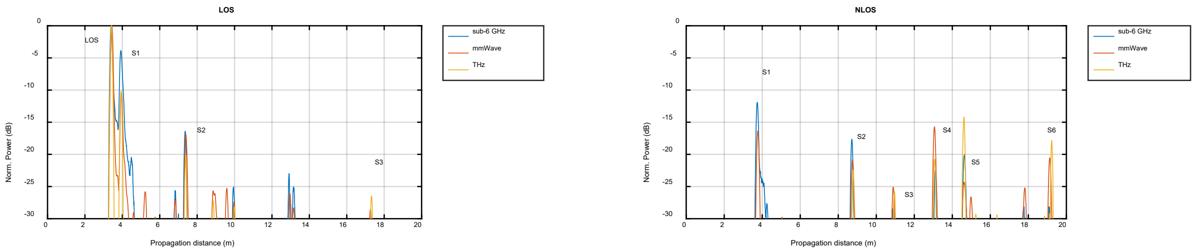

(a) Multiband power delay profile for the LOS link TX1-RX1. *(b) Multiband power delay profile for the NLOS link TX1-RX4.*

Figure 11 Multiband synthetic omni-directional power delay profile

To confirm the scattering sources, the ray-tracing simulations for the LOS link Tx1 – Rx1 and NLOS link Tx1 – Rx4 are displayed together in Figure 12 with the labels of the identified scatterers in the measurements.

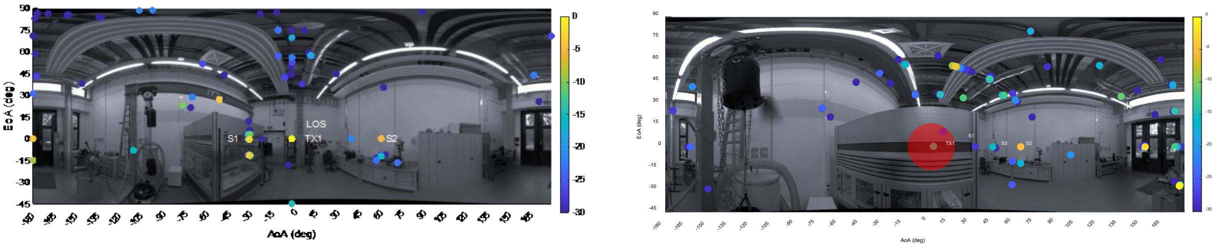

(a) Ray-tracing simulations for the LOS link TX1-RX1 *(b) Ray-tracing simulations for the NLOS link TX1-RX4*

Figure 12 Ray-tracing simulations for the links under investigation

5.1.2. Large-scale parameters for stochastic channel modelling

For the sake of a fair comparison, the dynamic range of the synthetic omni-directional power delay profiles was limited to 20 dB or the lowest dynamic over the different bands for the calculation of the delay spread (DS). The DS in LOS and NLOS are displayed in Figure 13. There is no clear relationship between frequency and the values. However, they follow similar trends in different positions. On average, a larger DS is observed at higher frequencies. The effects of a higher penetration loss and less diffracted power with increasing frequency, as seen in the PDP in Figure 10(b), generates early arriving paths that are only present in the lower bands. On the other hand, the relative size of objects to wavelength, e.g., the frames of windows and tools, makes some paths relatively stronger in the higher bands, for example, S4, S5 and S6 in Figure 10(b). The combination of these effects influences drastically the values of the LSPs over frequency.

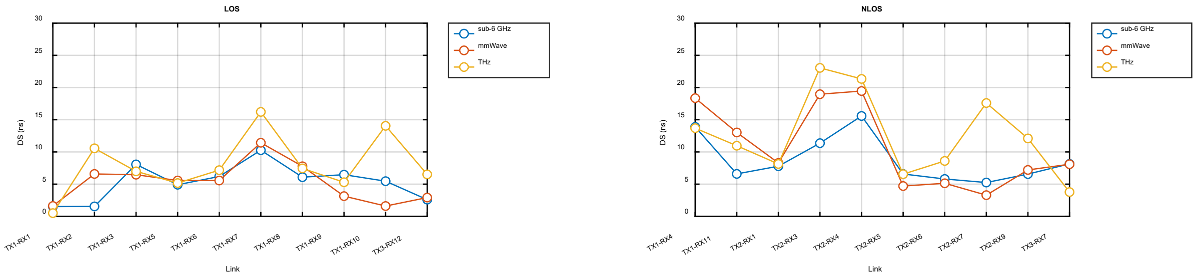

(a) Multiband delay spread for the LOS links *(b) Multiband delay spread for the NLOS links*

Figure 13 Multiband DS in LOS and NLOS

Similar results are observed with the azimuth spreads of arrival and departure in Figure 14 and Figure 15, respectively.

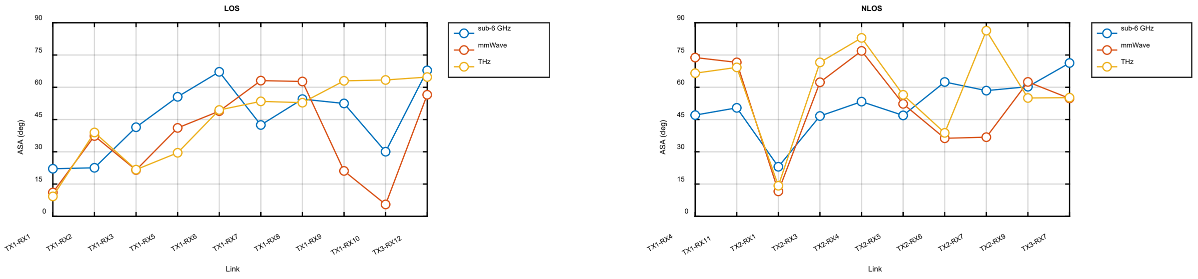

(a) Multiband azimuth spread of arrival for the LOS links *(b) Multiband azimuth spread of arrival for the NLOS links*

Figure 14 Multiband ASA in LOS and NLOS.

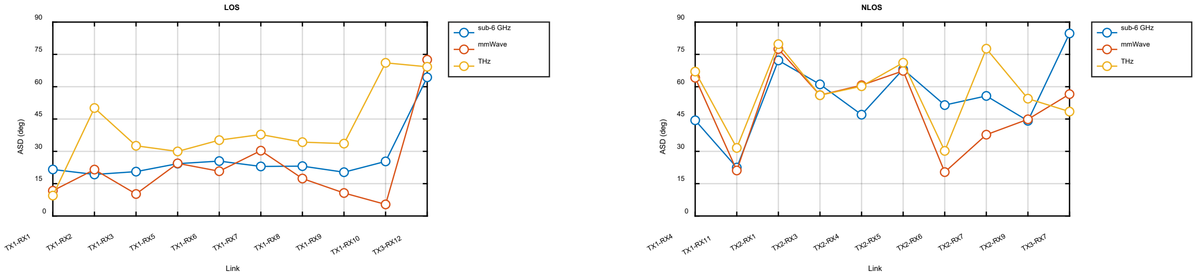

(a) Multiband azimuth spread of departure for the LOS links. *(b) Multiband azimuth spread of departure for the NLOS links.*

Figure 15 Multiband ASD in LOS and NLOS

Based on the channel measurement results close-in free space reference distance (CI) and alpha-beta-gamma (ABG) path loss models were fitted. CI and ABG path loss models are given by, respectively,

$$\mathrm{PL}^{\mathrm{CI}}\ [\mathrm{dB}] = 10 \cdot \mathrm{PLE} \cdot \log_{10}\left(\frac{d}{d_0}\right) + \mathrm{FSPL}(d_0) + X_\sigma^{\mathrm{CI}},$$

$$\mathrm{PL}^{\mathrm{AB}}\ [\mathrm{dB}] = 10 \cdot \alpha \cdot \log_{10}(d) + \beta + X_\sigma^{\mathrm{AB}},$$

where *d* denotes the distance in meters between Tx and Rx, and d_0, represents the reference distance of 1 meter. PLE is the path loss exponent, where α describes the dependence of the path loss on the distance between the transmitter and the receiver, β is a floating offset value of the path loss in dB, γ shows the dependence of the path loss on the frequency. *X* is a zero-mean Gaussian random variable with standard deviation *σ*. Free-space path loss (FSPL) in decibels (dB) is given by the Friis' law as

$$\mathrm{FSPL}(d)\ [\mathrm{dB}] = 20 \cdot \log_{10}\left(\frac{\lambda}{4\pi d}\right),$$

where λ is the carrier wavelength and d is the distance, both in meters.

The pathloss parameters for CI model (single and multi-band) were estimated for the LOS and NLOS positions and are summarized in Table 4. The individual per-band pathloss exponents show an increasing exponent with frequency, both in LOS and NLOS cases. The multi-band CI parameters in Table 4 were calculated across the three frequencies (Sub-6 GHz, mmWave, and THz) and represent the best fit values of parameters in terms of the mean-squared error.

Table 4. Single and multi-band close-in (CI) pathloss exponents (PLE) and standard deviation sigma (in dB) from multiband measurements

	Band	**PLE**	***σ***
LOS	Sub-6 GHz	2.11	1.06
	mmWave	2.21	1.31
	THz	2.26	1.51
NLOS	Sub-6 GHz	3.03	6.12
	mmWave	3.11	7.51
	THz	3.27	7.32
LOS	Multi-band	2.19	1.35
NLOS	Multi-band	3.13	6.81

Similarly, the ABG model was parametrized from the measurements. In NLOS, the large variations observed in the measurements in Figure 16 and short range generates unreliable ABG parameters for the NLOS situations, therefore, they are not listed. As can be seen in the results, early arriving paths tend to have a decreased gain with increasing frequency. Furthermore, there are higher penetration losses and less diffracted power with increasing frequency, and late arriving MPCs tend to have an increase in gain with frequency, because the farther objects (frames of windows, doors, machines) act as specular reflectors at higher frequencies and diffuse at lower frequencies.

Table 5. Current 3GPP and ITU-R models and empirical ABG pathloss parameters

Model	**Visibility**	***α***	***β***	***γ***	***σ***
3GPP TR.38901 InF-SL	LOS	2.15	31.84	1.9	4.3
	NLOS	2.55	33	2	5.07

ITU-R P.1238-11	LOS	2.31	24.52	2.06	2.69
	NLOS	3.79	21.01	1.34	9.05
Empirical parameters based on TIMES measurements	LOS	2.19	31.09	2.06	1.22

The empirical pathloss models, the measured path loss, and the 3GPP [10] and ITU [11] models are displayed in Figure 16. The 3GPP TR 38.901 model showed a better fit to the measurements in comparison to the ITU-R P.1238-11, especially in NLOS. Larger variations in the RX power can be seen with increasing frequency, as evidenced by the shadow fading parameter.

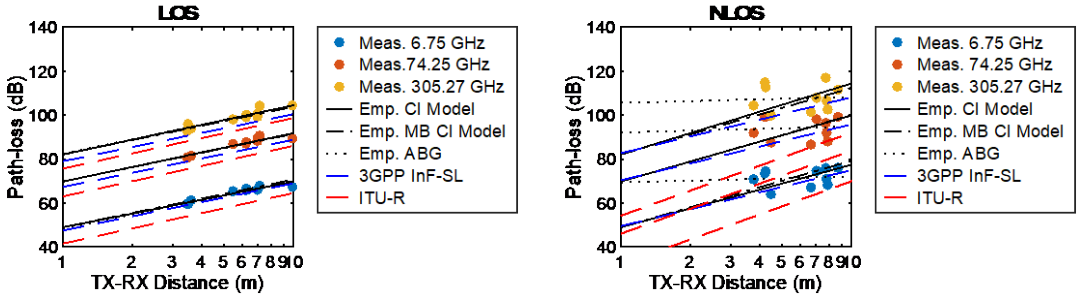

(a) Empirical multi-band pathloss in LOS. *(b) Empirical multi-band pathloss in NLOS.*

Figure 16. Empirical multi-band pathloss and the model for LOS and NLOS in short-range small industrial room scenario

5.2. Inter-device scenarios

The milling machine depicted in Figure 17 (outside) and Figure 18 (inside) was used in inter- and intra-device scenarios. The structure of the machine consists of metal frames and side, metallic and glass walls. Inside the machine, there are multiple components made of metal. The milling head has an XY positioner with two axes. Multiple metal holders are located on the ground of the inner part of the machine.

5.2.1. Medium machines: static conditions

5.2.1.1. Milling machine: inter-device–HWDU

In the case of inter-device scenarios, the Rx is placed inside the milling machine, whereas the Tx is outside of the machine. Figure 17 shows the view from the Tx, with the Rx being placed in several locations inside the machine, with the resulting Tx-Rx distance of 150 cm - 200 cm. This scenario depicts a small THz indoor base station communicating with a sensor/controller inside of a machine.

Figure 17 Environment for inter-device scenario with milling machine

The Power Angular Elevation Profile (PAEP) and Power Angular Delay Profile (PADP) at Tx and Rx for the different positions are shown in Figure 18 and Figure 19. In LOS conditions, multiple reflections on the frames of the machine can be observed apart from the direct component.

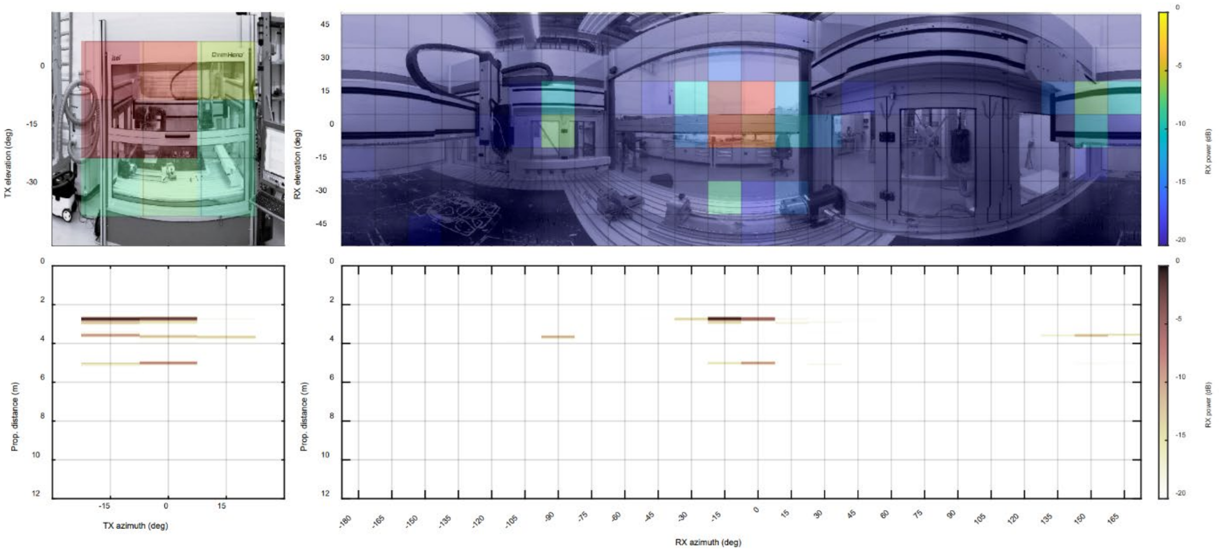

Figure 18 PAEP and PADP in LOS

The OLOS is obtained by opened frame of the protective window. The strongest component is a reflection from the axes of the milling head from the rear part. The new position of the window frame creates a new high order reflection rear frame/front frame of the window/rear positioner axis.

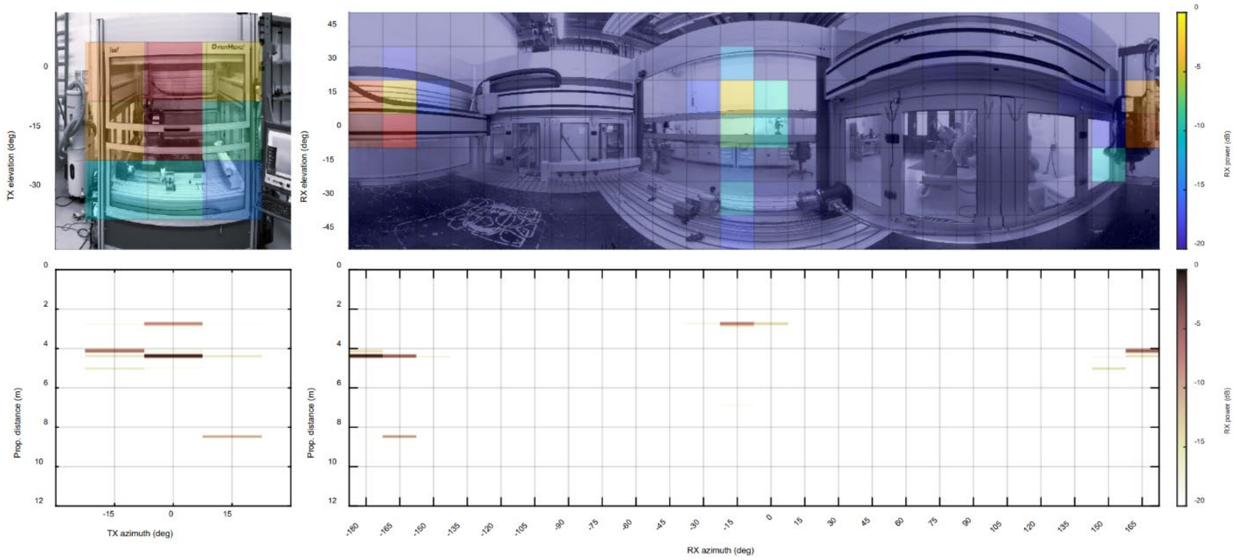

Figure 19 PAEP and PADP in OLOS

The synthetic omni-directional power delay profile in the different polarizations is displayed in Figure 20 and Figure 21. It can be noticed that stronger reflections correspond to the vertical polarization both in LOS and OLOS conditions.

Table 6 summarizes the channel parameters extracted from the measurements.

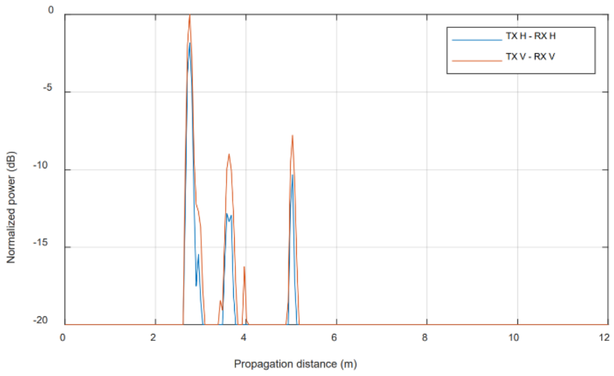

Figure 20 Polarimetric PDP in LOS

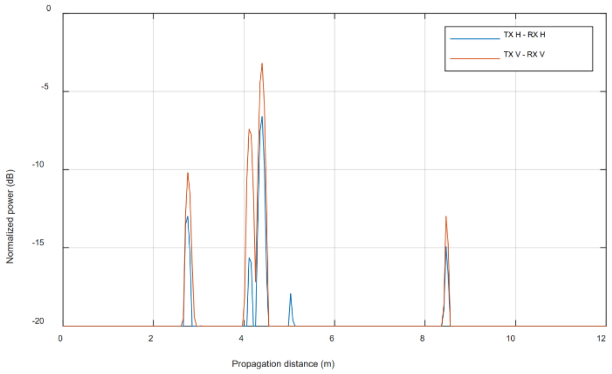

Figure 21 Polarimetric PDP in OLOS

Table 6 List of parameters from measurements gain in dB, delay spread (DS) in ns, azimuth angular spread of arrival (ASA), azimuth angular spread of departure (ASD), elevation angular spread of arrival (ESA), and elevation angular spread of departure (ESD), all in degrees (°).

Configuration	Visibility	Gain[1] (dB)	DS[2] (ns)	ASA (°)	ESA (°)	ASD (°)	ESD (°)
Axes of the milling head close to the RX, milling head on the left side of the RX	LOS	-89.29	2.36	63.43	15.99	9.59	8.92
Axes of the milling head in the middle of the machine, milling head in the middle	LOS	-89.04	7.04	89.69	16.51	9.66	9.35
Axes of the milling head in the rear of the machine, milling head in the left side	LOS	-89.54	3.90	87.31	11.99	9.88	8.18
Axes of the milling head in the rear of the machine, milling head in the left side Obstruction by frame of protective window	OLOS	-93.21	4.71	69.68	14.46	8.66	8.84

[1] *Isotropic channel gain: averaged over Tx angular scans and summed over Rx angular scans*

[2] *Calculated with 20 dB dynamic range*

5.2.1.2. Mono/bi-static sensing – HWDU

For this scenario, communications-only THz sensors (S), ISAC access points (APs) and user equipment (UEs) in the same industrial workshop environment shown in Figure 5. They can connect via machine-to-machine (M2M) links (e.g., AP1 to AP3) and/or as an external AP to inside of machine link (e.g., AP1 to the UE located inside of the production machine, addressed in Figure 5). The focus in this scenario is on utilization of the THz for sensing. Firstly, purely as bi-static sensors located at a low height (S1 and S2), and secondly as ISAC APs that scan the environment under the assumption of full-duplex capabilities, in which the AP1 transmits a sequence that the AP2 receives to picture the environment from the estimated CIR, to detect, for example, the proximity and trajectory of a forklift truck which will interrupt the link AP1-UE.

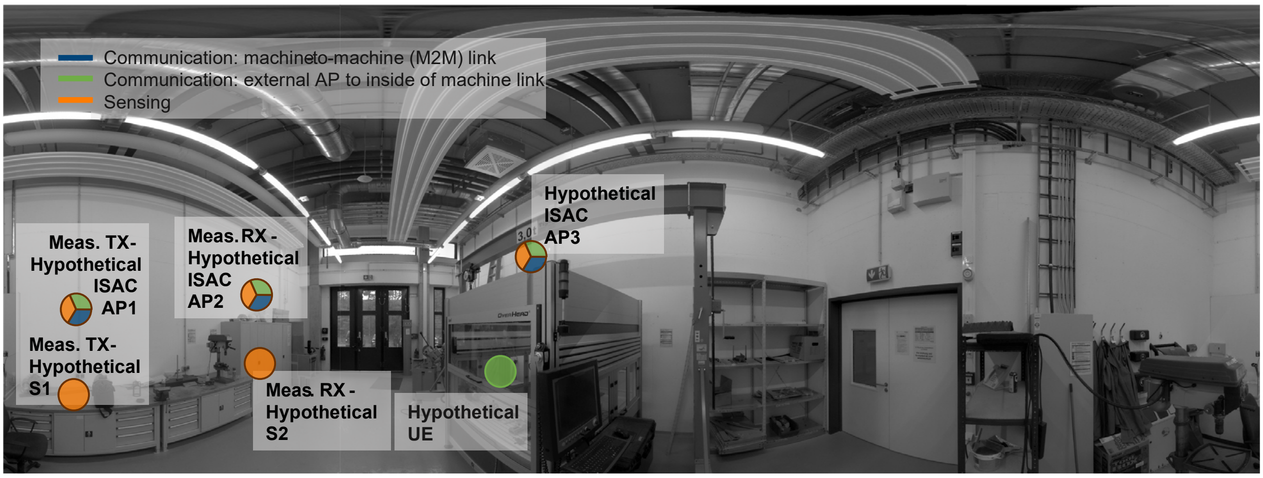

Figure 22 360° picture of the scenario and the location of the measurement TX and RX and the hypothetical location of the APs, sensors, and UE

The overall scenario is shown in Figure 22 and consists of a machine hall (6.48 m⇥10.05 m⇥6.33 m) with different tools typically found in industrial and machine halls. The predominant constructive materials of the different items are iron, steel, aluminium, plexiglass, concrete, and steel sheet. This scenario can be compared to a portion of a production line. The machine of interest is located in the centre of the hall, a computer numerically controlled (CNC) milling machine.

5.2.1.2.1. Experimental Set-up

Due to the current state of the art on channel sounding at THz using mechanically rotated high gain antennas to capture the angular dimension of the channel, it is not possible to simultaneously resolve angle of departure and arrival in dynamic scenarios. Therefore, the emulation of the dynamic situation of a moving target in the environment (forklift truck) was recreated by manually displacing the target over a 5 m long track *d* parallel to the Tx-Rx line and repeating the measurements for each new position.

Two different set-ups were defined: *purely sensing* and *integrated sensing and communications access point* scenario. The first one was designed to capture the maximum reflection from the body of the forklift truck since the Tx, Rx, and target are in the same horizontal plane. Hence, there is no need of scans in the elevation domain, reducing measurement time and allowing a finer grid on the displacement of the truck. However, the location of the Tx and Rx corresponds more to a RADAR application than to communications. On the other hand, the Tx and Rx are located at a realistic height for communications in the set-up with a high access point scenario. However, this requires scans in the elevation domain which increases considerably the measurement time. Thus, for this scenario, only two positions of the forklift truck were measured: without and with the forklift truck. This set-up is used as a validation of the proof of concept.

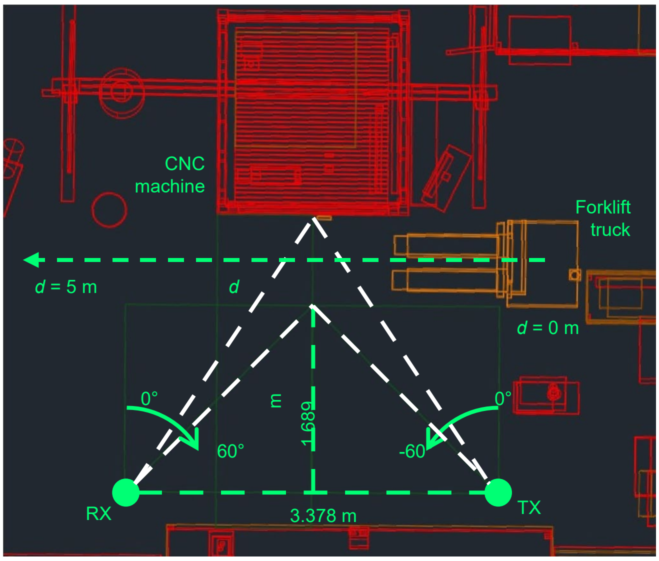

Figure 23 Schematic of the measurement set-up showing the location of the Tx, Rx, CNC machine, and the track of the forklift truck

The measurement set-up for both cases is described in Figure 23. The Tx and Rx were located at 3.378 m distance from each other.

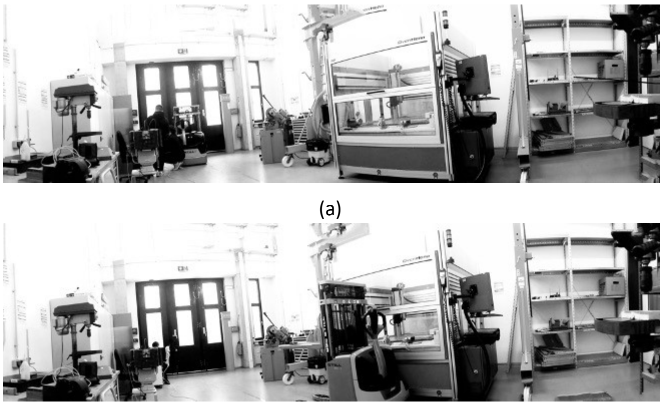

(a)

(b)

Figure 24 Composite picture taken by the TX of the channel sounder in the low access point scenario at 1 m height (a) without fork-lift truck, and (b) with forklift truck in the middle obstructing the link to the CNC machine.

1) Purely Sensing Scenario: The Tx and Rx were located at a 1 m height, as pictured in Figure 24. This height was chosen to capture the worst-case scenario of blockage and the maximum reflection of the body of the target. The forklift truck was displaced with 15 cm steps over the 5 m long track with a total of 33 measurement positions. The Tx scanned in azimuth from 0 to 60 and The Rx from 0 to 60 with 15 steps, as shown in Figure 24.

2) Integrated Sensing and Communications Access Point Scenario: The Tx and Rx were located in the same positions as in the previous experiment, but at a height of 2 m emulating a realistic location for an AP. The measurements were repeated considering also scans in the elevation: the Tx and Rx swept the azimuth from 60 to 0 and from 0 to 60, respectively, and the elevation from 45 to 0 with 15 steps. However, due to measurement time, only two different positions of the forklift truck over the track *d* were measured: no truck, and the truck obstructing the specular reflection in the CNC machine.

5.2.1.2.2. Analysis of the Measurement Results

5.2.1.2.2.1. Pure Sensing Scenario

The synthetic isotropic power of the measured CIR is displayed in Figure 25 for the vertical-to-vertical polarization for the different positions d of the forklift truck over the 5 m length track Figure 25.

The reflection on the CNC machine is observed as the peak with a propagation distance of approximately 6.5 m. The presence of the forklift truck in the position d = 0 m is observed as the two peaks with propagation distance of approx. 5.7 and 6.25 m. These peaks describe the elliptic trajectory while the forklift truck is displaced parallel to the Tx-Rx line. The maximum blockage of the hypothetical AP-UE link occurs when the forklift truck is in the position d = 2.2 m where the reflection from the CNC machine is completely blocked.

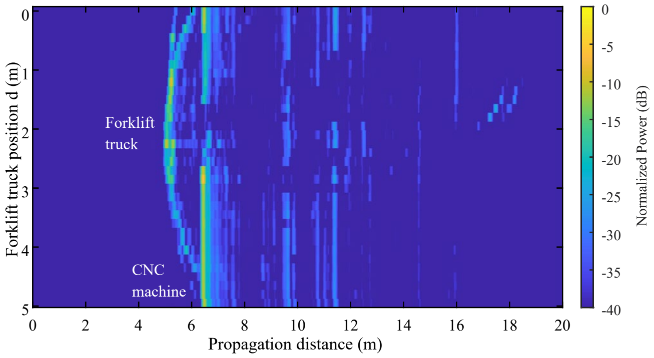

Figure 25 Synthetic omni-directional power of the CIR for the different positions of the forklift truck in the track d in the purely sensing scenario

5.2.1.2.2.2. Integrated Sensing and Communications Access Point Scenario

The power for the different azimuth and elevations at the Tx for the case without and with forklift truck are displayed in Figure 26 (a) and Figure 26 (b), respectively. Due to the new geometry in the scenario, the strongest reflection off the CNC machine comes from the upper frame, which is not blocked by the forklift truck. In addition, a strong specular reflection is also observed from the lower part of the CNC machine in the power azimuth and elevation profile in Figure 26 (b) at Tx azimuth and elevation scans (φ, ϑ) = (-30° , -15°degree). This defines the background picture, or the normal situation of the hall. With the forklift truck in the scenario, the reflection from the lower frame of the machine is blocked as seen in Figure 26 (b), but there is a new component arriving from the forklift truck. With the new geometry, the reflection in the forklift truck is not specular anymore since there is no surface perpendicular to the plane containing the reflected path.

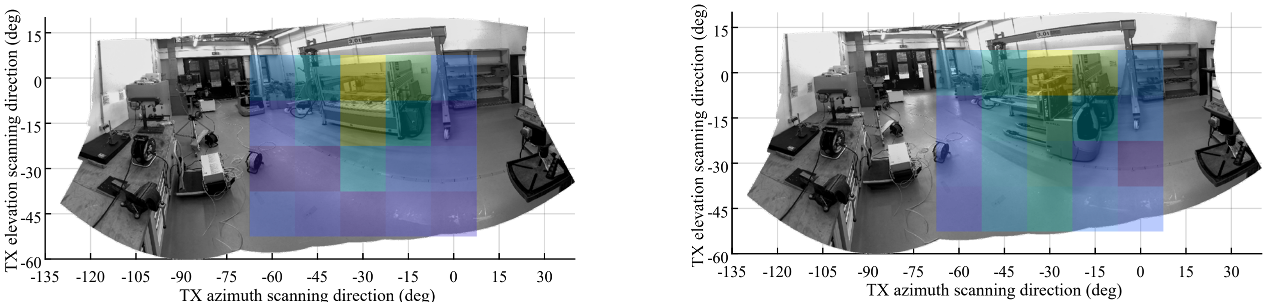

(a) *(b)*

Figure 26 Composite picture taken by the TX of the channel sounder with the measured power for the different azimuth and elevation scans at the TX in the ISAC AP scenario for (a) no forklift truck, and (b) forklift truck in the middle obstructing the link

5.2.1.3. Big industrial workspace: access point – TUBS

The “access point” scenario represents THz transmission between an access point and a sensor on a machine in the comprehensive industrial environment.

5.2.1.3.1. Experimental Setup

The setup was constructed as follows: Tx is fixed on the tripod and located on the upper level of the industrial space. Two Rx units are fixed on the tripods and located on the lower level of the workspace, on opposite sides of the massive machine. Schematic views of the setup are presented in Figure 27.

The setup parameters are presented in Table 7, where h_{TX}, h_{RX} are Tx and Rx heights; $d_{TX\text{-}W1}$ is the distance between Tx and Wall 1; $d_{RX1\text{-}W1}$ is the distance between Rx1 and Wall 1; $d_{RX2\text{-}W1}$ is the distance between Rx2 and Wall 1; $d_{RXs\text{-}W2}$ is the distance between Rxs and Wall 2; α_{TX} and α_{RX} are the Tx and Rxs elevation angles (Figure 28(a)) and β_{TX} and β_{RX} are the Tx and Rxs azimuth angles (Figure 28(b)). Photos of the setups are presented in Figure 29.

Finally, measurements were conducted separately for Rx1 and then for Rx2. Two extreme cases were considered for both Rx units: when Tx and Rx were misaligned (Setups 1 and 12) and when they were fully aligned (Setups 11 and 22). Between these limit cases, several partially aligned setups were measured. Also, two different distances between Rxs and Wall 2 were investigated: 8 m and 6.5 m. All possible setup options are presented in Table 7.

(a)

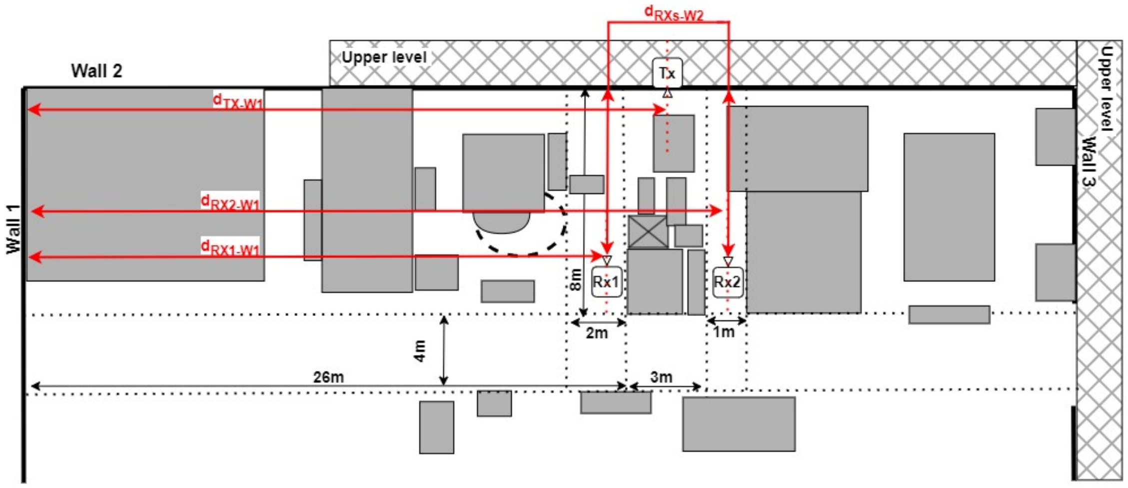

(b)

Figure 27 “Access point” scenario schematic views: (a) side view; (b) view from above

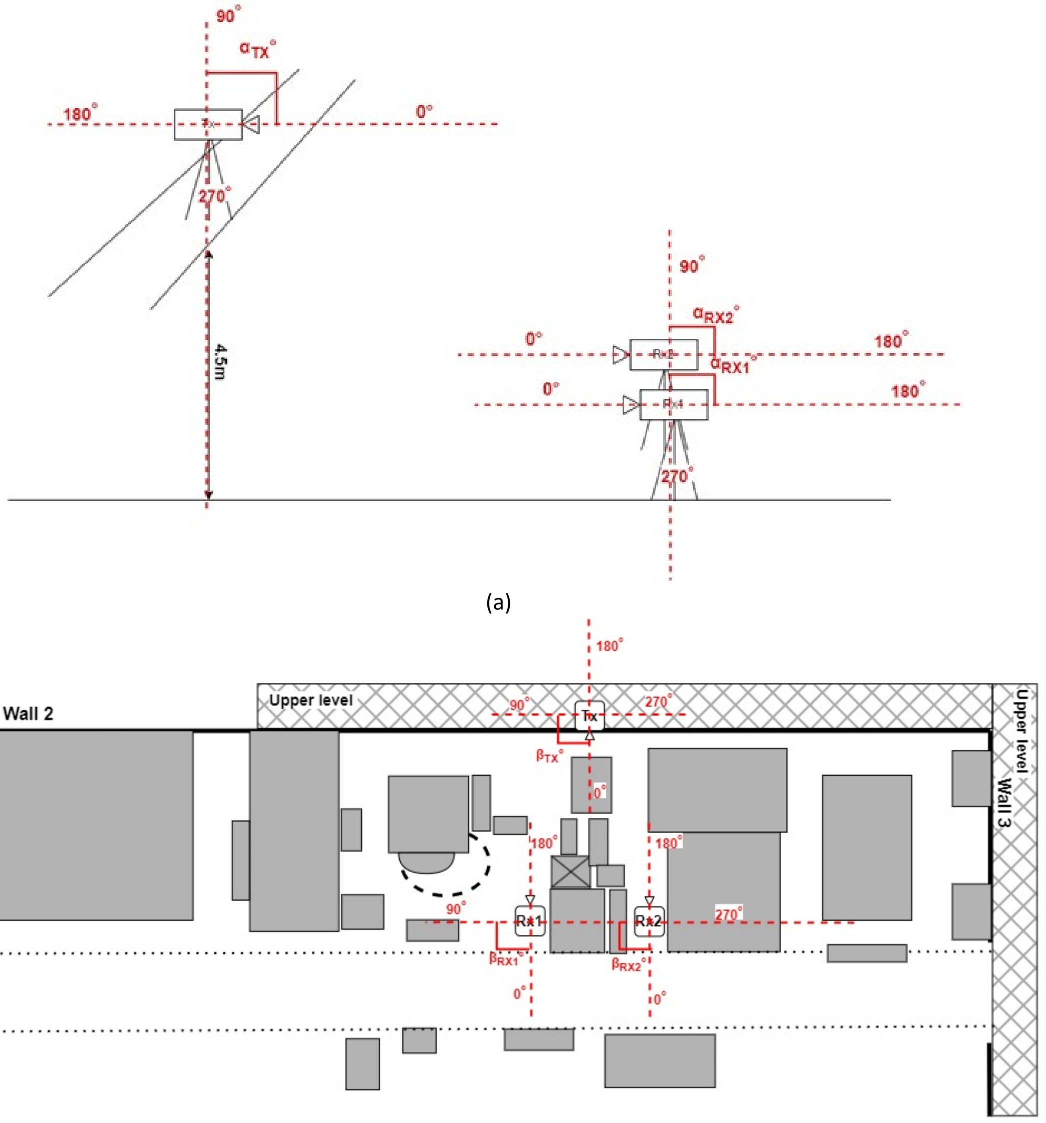

(a)

(b)

Figure 28 Angle direction description: (a) elevation angles; (b) azimuth angles

(a)

(b)

Figure 29 Measurement setup photos: (a) Tx and Rx1; (b) Tx and Rx2

Table 7 Access point setups parameters

Setup number	**Rx number**	**h_{Tx}, m**	**h_{Rx}, m**	**d_{Tx-W1}, m**	**d_{Rx1-W1}, m**	**d_{Rx2-W1}, m**	**d_{Rxs-W2}, m**	**A_{Tx}°**	**$\alpha_{Rx1,2}$°**	**β_{Tx} °**	**β_{Rx1}°**	**β_{Rx2}°**
1	1	5.26	1.25	21.7	19	24.5	8	0	0	0	180	–
2	1	5.26	1.25	21.7	19	24.5	8	-35	35	0	180	–
3	1	5.26	1.25	21.7	19	24.5	8	-35	0	5	180	–
4	1	5.26	1.25	21.7	19	24.5	8	-35	0	15	180	–
5	1	5.26	1.25	21.7	19	24.5	8	-35	0	25	180	–
6	1	5.26	1.25	21.7	19	24.5	8	-35	0	15	185	–
7	1	5.26	1.25	21.7	19	24.5	8	-35	0	15	195	–
8	1	5.26	1.25	21.7	19	24.5	6.5	-35	0	15	195	–
9	1	5.26	1.25	21.7	19	24.5	6.5	-35	0	15	205	–
10	1	5.26	1.25	21.7	19	24.5	6.5	-35	35	15	195	–
11	1	5.26	1.25	21.7	19	24.5	8	-35	35	15	195	–
12	2	5.26	1.25	21.7	19	24.5	8	0	0	0	–	180
13	2	5.26	1.25	21.7	19	24.5	8	-35	35	0	–	180
14	2	5.26	1.25	21.7	19	24.5	8	-35	0	5	–	180
15	2	5.26	1.25	21.7	19	24.5	8	-35	0	15	–	180
16	2	5.26	1.25	21.7	19	24.5	8	-35	0	25	–	180
17	2	5.26	1.25	21.7	19	24.5	8	-35	0	15	–	175
18	2	5.26	1.25	21.7	19	24.5	8	-35	0	15	–	165
19	2	5.26	1.25	21.7	19	24.5	6.5	-35	0	15	–	165
20	2	5.26	1.25	21.7	19	24.5	6.5	-35	0	15	–	155
21	2	5.26	1.25	21.7	19	24.5	6.5	-35	35	15	–	165
22	2	5.26	1.25	21.7	19	24.5	8	-35	35	15	–	165

5.2.1.3.2. Measurement evaluation and results

Each obtained CIR was calibrated using a Back-to-Back (B2B) calibration and deconvolution procedure. In B2B calibration, the Tx and Rx are directly connected through waveguides, bypassing the propagation path, which allows the system's intrinsic delay, amplitude response, and gain characteristics to be measured and accounted for. This process, combined with deconvolution to remove system influences from the received signal, ensures that the resulting CIR retains only the propagation path characteristics, isolating the path gain (PG) without including system-specific gains. Therefore, the calibrated CIR refers to the PG, which quantifies the decrease in signal strength as it travels from the Tx to the Rx and is measured in decibels (dB).

The calibrated CIR matrices were used to create each measured PDP. The root mean square Delay Spread (rms DS) were calculated from the measured PDPs. For calculating rms DS, a threshold of 6 dB above the noise was chosen. The noise floor was estimated and had value -167 dB, setting the noise cut-level at -161 dB. PG and DS values for each set up are presented in Table 8.

The PDP are presented in Figure 30 – Figure 32, where only MPCs with PG higher than the noise cut-level are displayed to highlight the relevant MPCs and better illustrate environmental properties in terms of reflections and scattering effects.

In the case of Setup 1, when Tx and Rx1 were misaligned, there is no LOS component. However, MPCs set can be observed in delays between 150 ns and 175 ns, with the strongest component PG = -141.7 dB. These MPCs components can be described as reflections from the opposite wall and then from machine between receivers. The main reflected in described MPCs set is stronger than LOS component that appeared in Setup 2, when Tx and Rx are aligned in elevation plane, this LOS PG value is just -160.7 dB. Furthermore, the strongest component in Setup 2, is not LOS and has PG = -158.3 dB. In Setup 4, when Tx was aligned in both elevation and azimuth planes and Rx1 was not aligned at all, we can observe a weak LOS component (PG = - 160.1 dB) and set of MPCs between 55 ns and 70 ns with the strongest path gain value of -148.8 dB. This set of MPCs can be described by reflections from a massive machine located between Rx1 and Rx2. In Setup 11, where Tx and Rx1 were aligned in both elevation and azimuth planes, a strong LOS component exists with value - 117.4 dB. A comparison of those four setups PDP is presented in Figure 30 (a). The same setups, but for Rx2 is shown in the Figure 30 (b).

The comparison of the measured PDP for different distances between Rxs and Wall 2 (8 m and 6.5 m) shows a different number of MPCs, in addition to the obvious difference in the LOS time delay. 8 MPCs are observed when Rx1 was located at a distance of 8 m from Wall 2. On the other hand, 20 MPCs are observed when Rx1 is located at a distance of 6.5 m from Wall 2. A comparison of these MPCs and similar MPCs for Rx2 is shown in Figure 31.

It is also interesting to compare the PDPs of Rx1 and Rx2 in similar setups. This is shown in Figure 32Figure 33 which presents the PDPs of both receivers in extreme cases. In misaligned cases (Setup 1 and Setup 12) there are substantial MPCs sets with delays around 175 ns for both Rx units. However, in case of Rx2, the MPCs count is larger than for Rx1. Also, it is located between 150 ns and 225 ns, whereas for Rx1, the MPCs set is concentrated between 150 ns and 175 ns. It can be explained by the difference in the environment near Rx1 and Rx2. As seen in Figure 29 (b), there is a line of massive machines on both sides of Rx2 and mostly free space on the left side of Rx1, Figure 29 (a).

In setups 11 and 22, when Rx units are aligned with Tx, a difference in the LOS gain values between Rx1 and Rx2 can be observed. For Rx1, PG = -117.4 dB and PG = -100.6 dB for Rx2. The value obtained for the Rx2 setup agrees well with the computed gain for this distance. This difference can be explained by the fact that the massive machine located between Rx1 and Rx2 is slightly shifted toward Rx1 side and is partially obstructing the LOS. Thereby, it can be concluded that Setup 11 is an OLOS, and it has a difference of 16.8 dB in comparison with Rx2 LOS case.

Table 8 Measurement results

Setup number	**Rx number**	**PG, dB**	**rms DS, ns**
1	1	-141.7 (NLOS)	14.5
2	1	-158.3 (NLOS)	35.04
3	1	-158.4 (NLOS)	56.8
4	1	-148.8 (NLOS)	3.8
5	1	-159.3 (LOS)	0.1
6	1	-139.8(NLOS)	7.1
7	1	-135.3(LOS)	12.9
8	1	-143.1(NLOS)	11.5
9	1	-143.6(LOS)	0.2
10	1	-119.3(LOS)	10.9
11	1	-117.4(LOS)	12.4
12	2	-149.6(NLOS)	28.9

13	2	-138.9(LOS)	25.7
14	2	-155.4(NLOS)	17.9
15	2	-144.3(LOS)	18.4
16	2	-154.1(LOS)	17.2
17	2	-150.7(LOS)	0.2
18	2	-124.5(LOS)	10.3
19	2	-129.2(LOS)	7.3
20	2	-125.9(LOS)	14.1
21	2	-103.9(LOS)	16.7
22	2	-100.6(LOS)	12.4

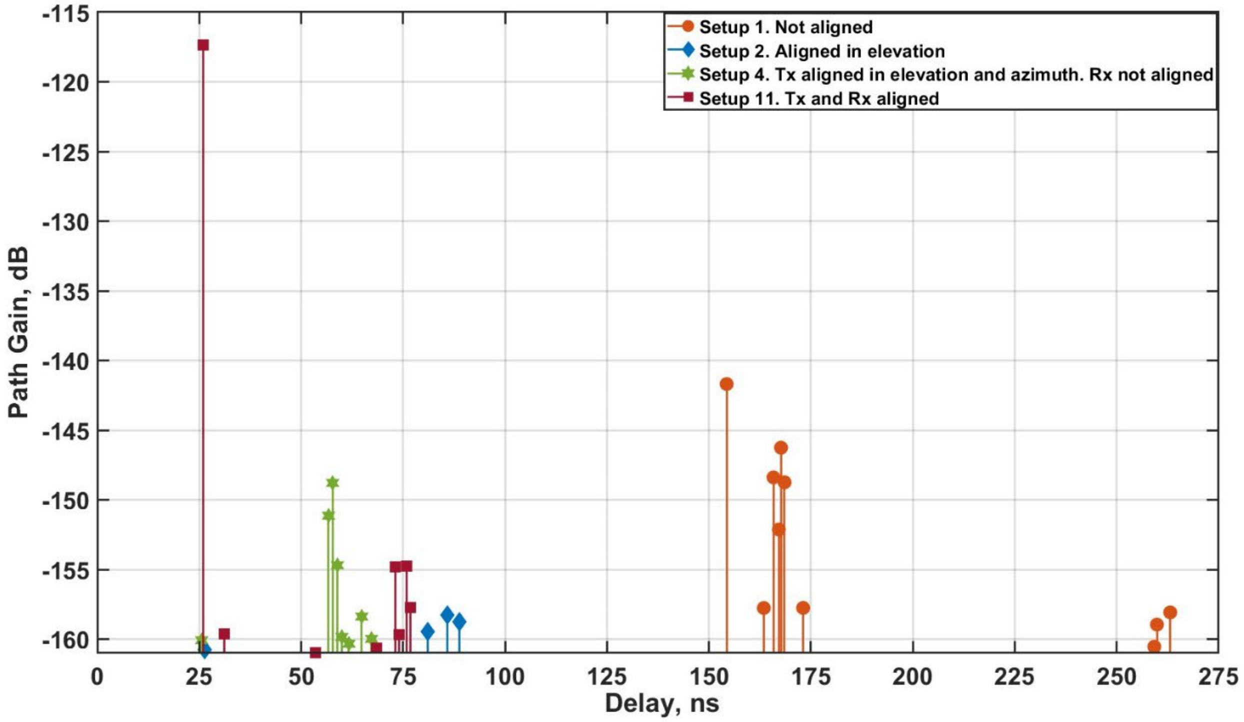

(a)

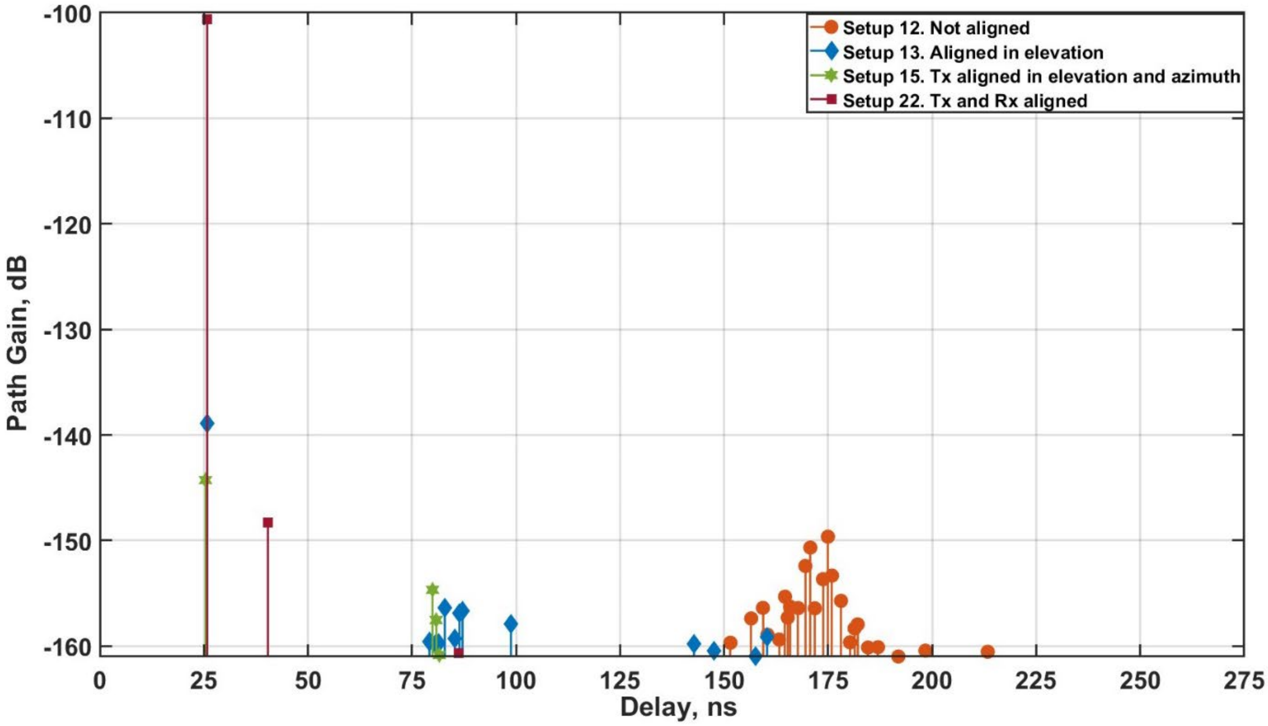

(b)

Figure 30 PDPs for different alignment levels: (a) for Rx1; (b) for Rx2

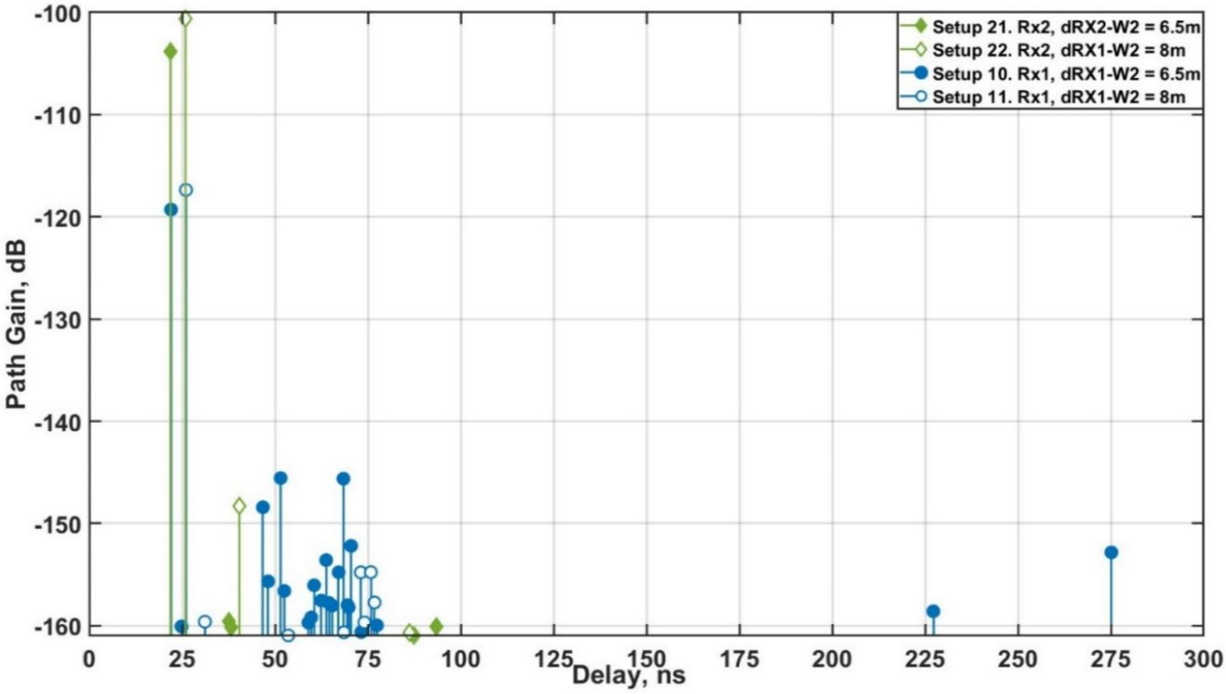

Figure 31 PDPs for $d_{RXs\text{-}W2}$ = 8 m and $d_{RXs\text{-}W2}$ = 6.5 m with both Rx units. Tx and Rx are aligned

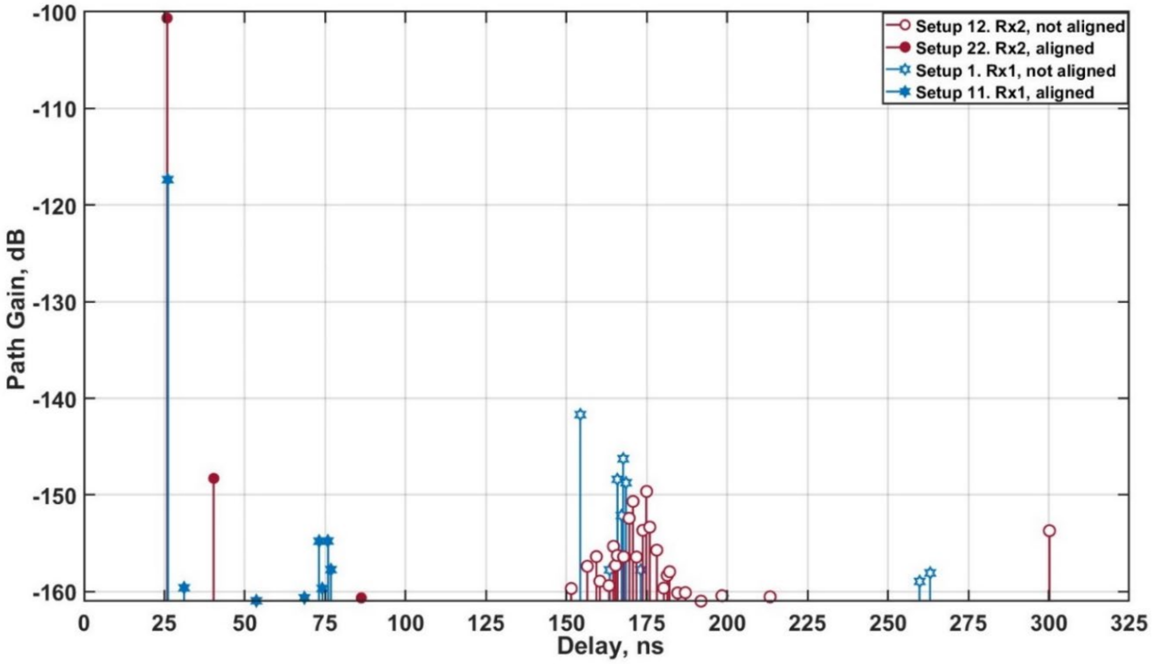

Figure 32 Rx1 and Rx2 PDPs comparison for the extreme cases when Tx and Rx fully aligned and misaligned

5.2.1.4. Robotic arms: access point – TUBS

This scenario represents a THz transmission between an access point and a sensor on the base of the robotic arm manipulator in the robotic laboratory workspace.

5.2.1.4.1. Experimental Setup

During the measurement setup, Tx and Rx units were positioned at the tripods. Tx (access point) was placed at a distance away from the robotic manipulator, while the Rx was positioned near the base of the robotic arm. The scenario involved three different Tx heights, with fixed Rx height. For each case when Tx and Rx heights were different, there were two options: one with misaligned Tx and Rx antennas, and the other with aligned antennas. Additionally, this scenario included three robotic arm configurations, as depicted in the schematic view in Figure 33. Hence, there was a grand total of 15 setups. All possible setup options are presented in Table 9. The setup configuration parameters are also presented in Table 9 h_{TX}, h_{RX} is Tx and Rx heights respectively, $d_{TX\text{-}RX}$ is the distance between Tx and Rx. Photos of the setup are presented in Figure 34.

To ensure the precise characterization of the robotic manipulator arms, reference measurements were conducted in identical setups but without the manipulator arms. Reference measurements allow to estimate the environment impact and separate it from the robotic manipulators impact.

Table 9 Setups' parameters

Setup number	h_{Tx}, m	h_{Rx}, m	$d_{Tx\text{-}Rx}$, m	Configuration number	Aligned/not aligned
1	1.09	1.08	4.08	1	aligned
2	1.09	1.08	4.08	2	aligned

3	1.09	1.08	4.08	3	aligned
4	1.3	1.08	4.08	1	not aligned
5	1.3	1.08	4.08	1	aligned, ±3°
6	1.3	1.08	4.08	2	not aligned
7	1.3	1.08	4.08	2	aligned, ±3°
8	1.3	1.08	4.08	3	not aligned
9	1.3	1.08	4.08	3	aligned, ±3°
10	1.6	1.08	4.08	1	not aligned
11	1.6	1.08	4.08	1	aligned, ±7°
12	1.6	1.08	4.08	2	not aligned
13	1.6	1.08	4.08	2	aligned, ±7°
14	1.6	1.08	4.08	3	not aligned
15	1.6	1.08	4.08	3	aligned, ±7°

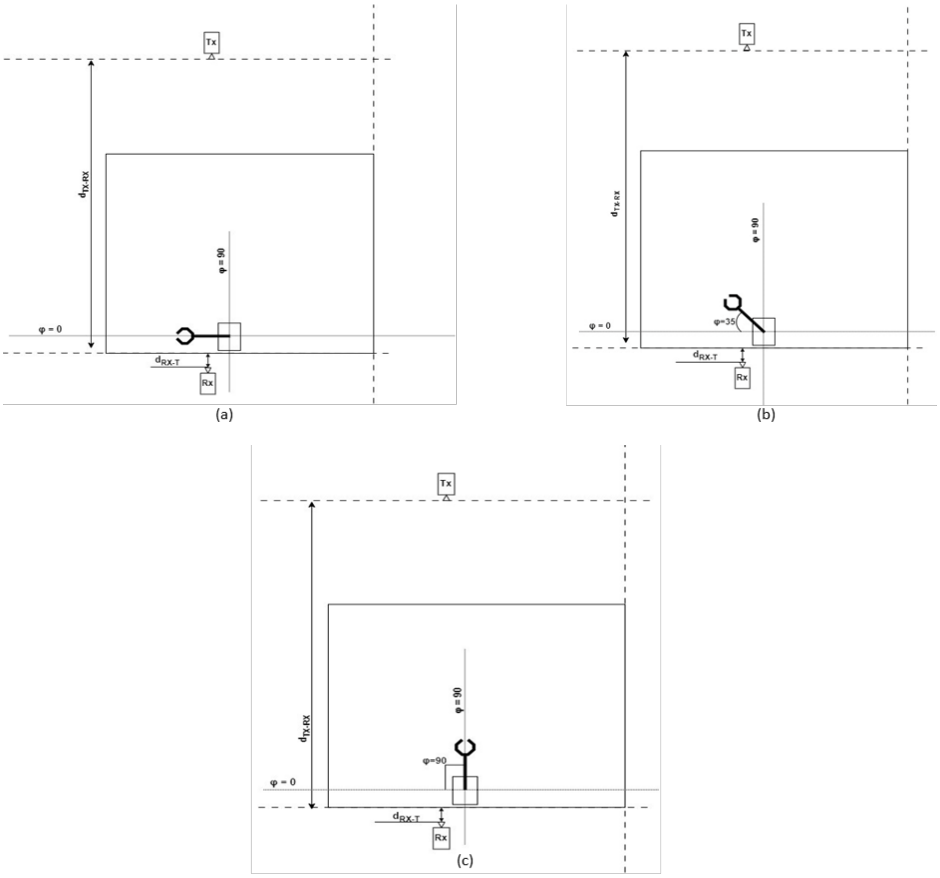

Figure 33 Schematic view from above for different arm configurations (a) Configuration 1, (b) Configuration 2, (c) Configuration 3

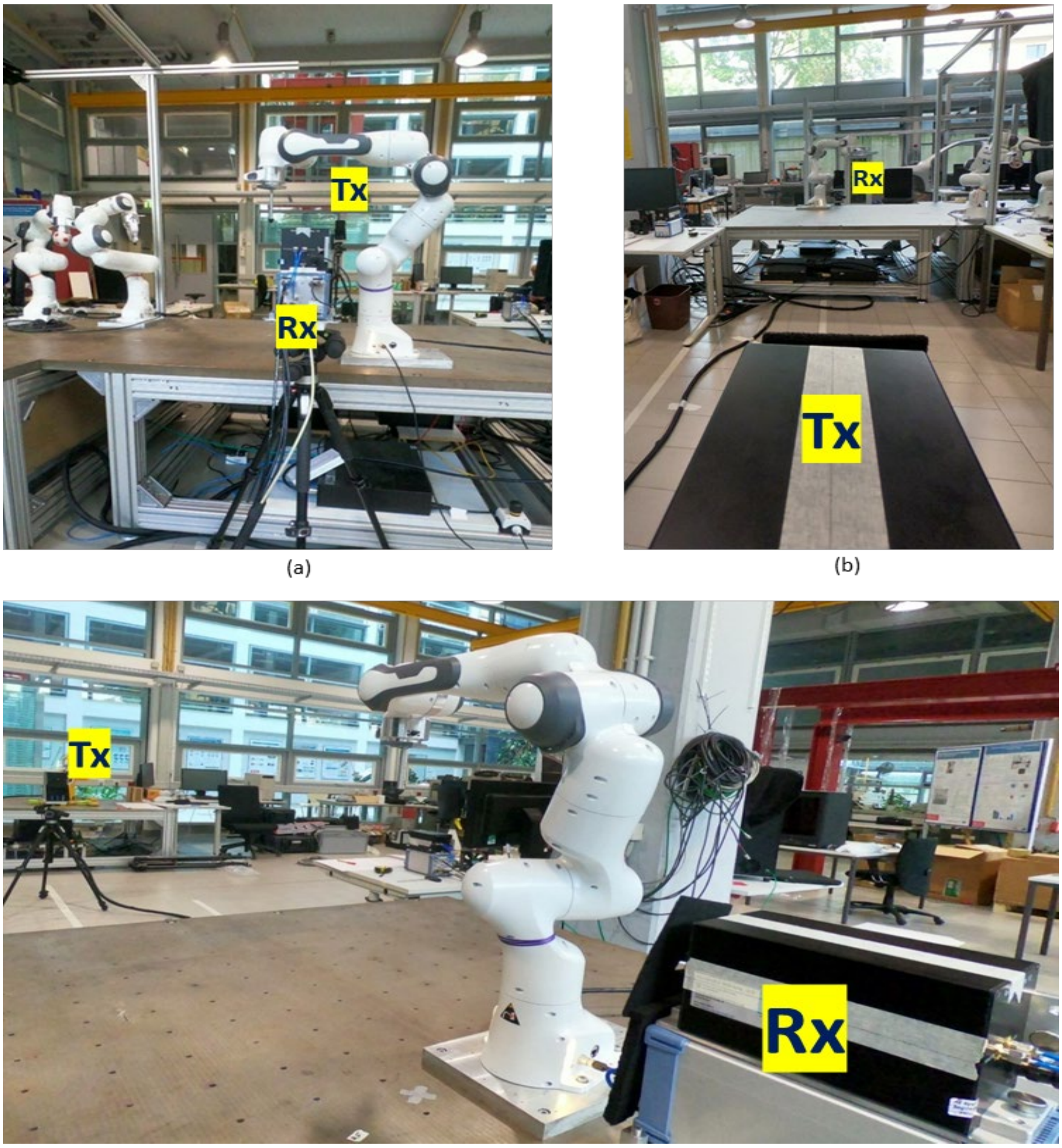

Figure 34 Photos of measurement setups with three different robotic manipulator configurations: (a) Configuration 1; (b) Configuration 2; (c) Configuration 3

5.2.1.4.2. Measurement evaluation and results

Each obtained CIR was calibrated in terms of path gain and delay using back-to-back (B2B) measurement performed before measurements and deconvolution procedure, like it was described in the previous section. Calibrated CIR matrices were used to create the measured PDP presented in Figure 35 – Figure 39. The analysis of the measurement results gave by PG (Table 10), and rms DS (Table 11). The noise floor level was -171 dB, and with threshold of 6 dB noise cut-level for DS calculation was -165 dB.

Table 10 Channel Gain for different Tx/Rx heights and robotic arm configurations

Heights, aligned/not aligned	**PG, dB**		
	Configuration 1	Configuration 2	Configuration 3
h_{TX} = 1.08 m; h_{RX} = 1.08 m	-97.5	-94.6	-95.2
h_{TX} = 1.3 m; h_{RX} = 1.08m (not aligned)	-99.3	-99.5	-97.9
h_{TX} = 1.3 m; h_{RX} = 1.08 m (aligned)	-95.8	-97.8	-97.3

h_{TX} = 1.6 m; h_{RX} = 1.08 m (not aligned)	-112.6	-111.1	-111.2
h_{TX} = 1.6 m; h_{RX} = 1.08 m (aligned)	-97.2	-95.4	-96.8

Table 11 Delay Spread for different Tx/Rx heights and robotic arm configurations

Heights, aligned/not aligned	**DS, ns**		
	Configuration 1	Configuration 2	Configuration 3
h_{TX} = 1.08 m; h_{RX} = 1.08 m	0.94	0.78	0.77
h_{TX} = 1.3 m; h_{RX} = 1.08m (not aligned)	2.93	3.29	3.36
h_{TX} = 1.3 m; h_{RX} = 1.08 m (aligned)	1.86	1.96	2.09
h_{TX} = 1.6 m; h_{RX} = 1.08 m (not aligned)	12.23	9.29	8.17
h_{TX} = 1.6 m; $_{hRX}$ = 1.08 m (aligned)	0.6	0.59	0.54

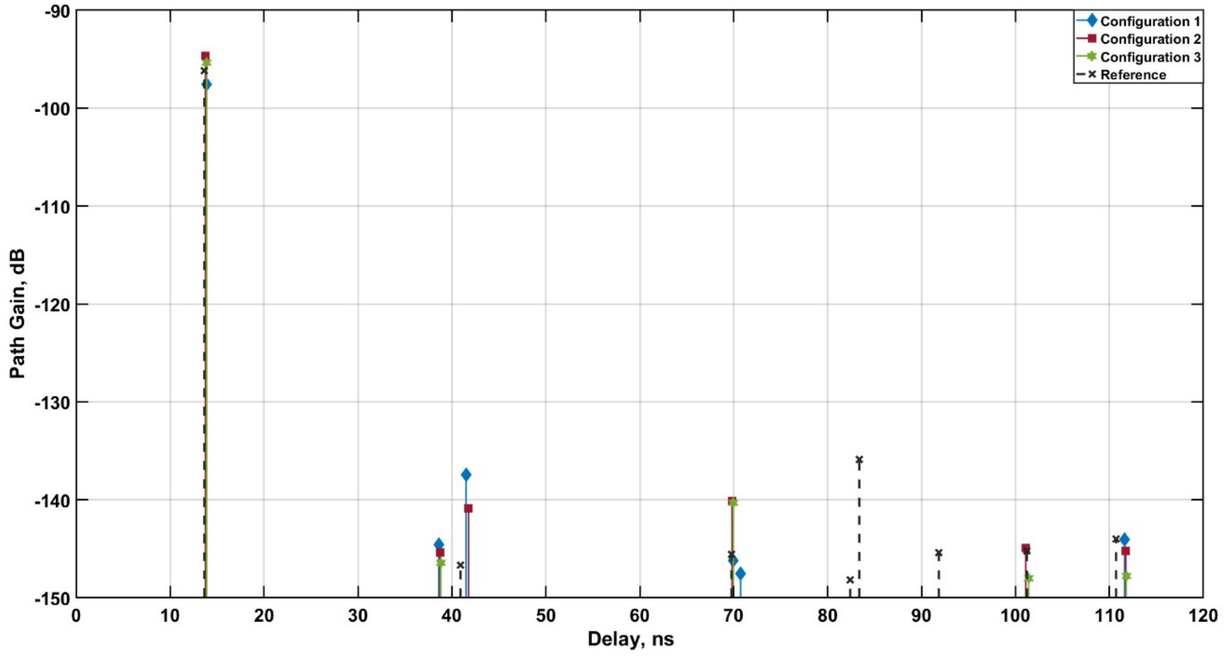

Figure 35 PDP for h_{Tx}=1.09m and h_{Rx}=1.08m for three different robotic arm configurations (Setups 1–3). The reference measurement is without the robotic arm

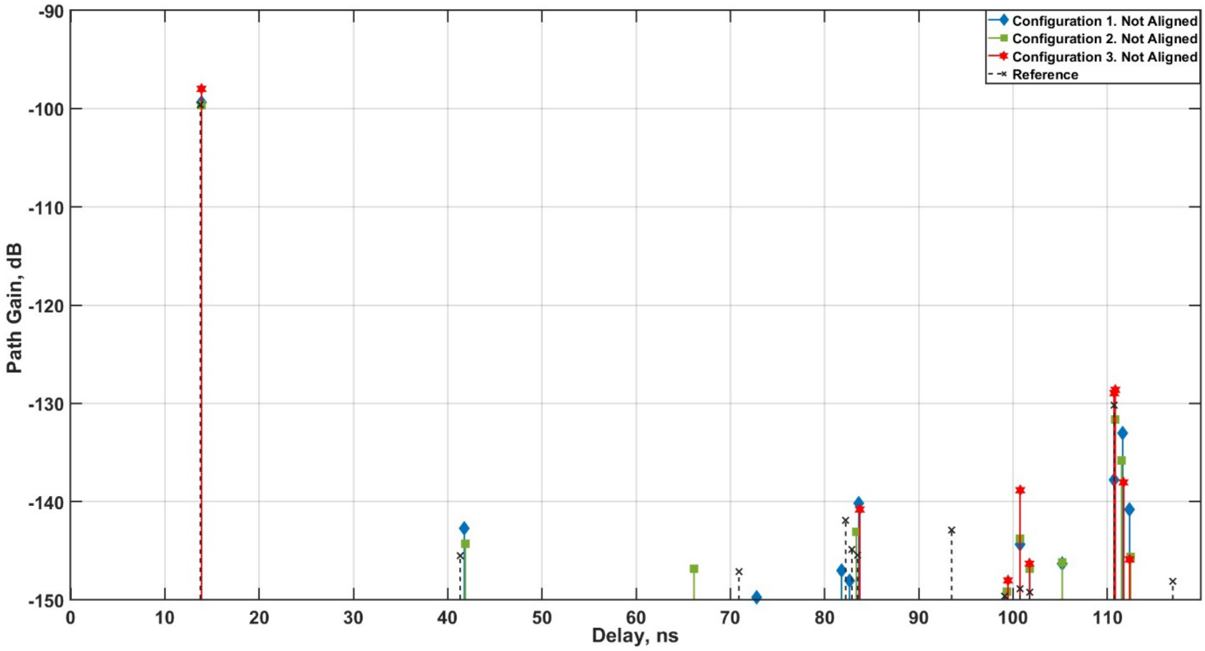

Figure 36 PDP for h_{Tx}=1.3m and h_{Rx}=1.08m and not aligned Tx and Rx, for three different robotic arm configurations (Setups 4, 6 and 8). The reference measurement is without the robotic arm

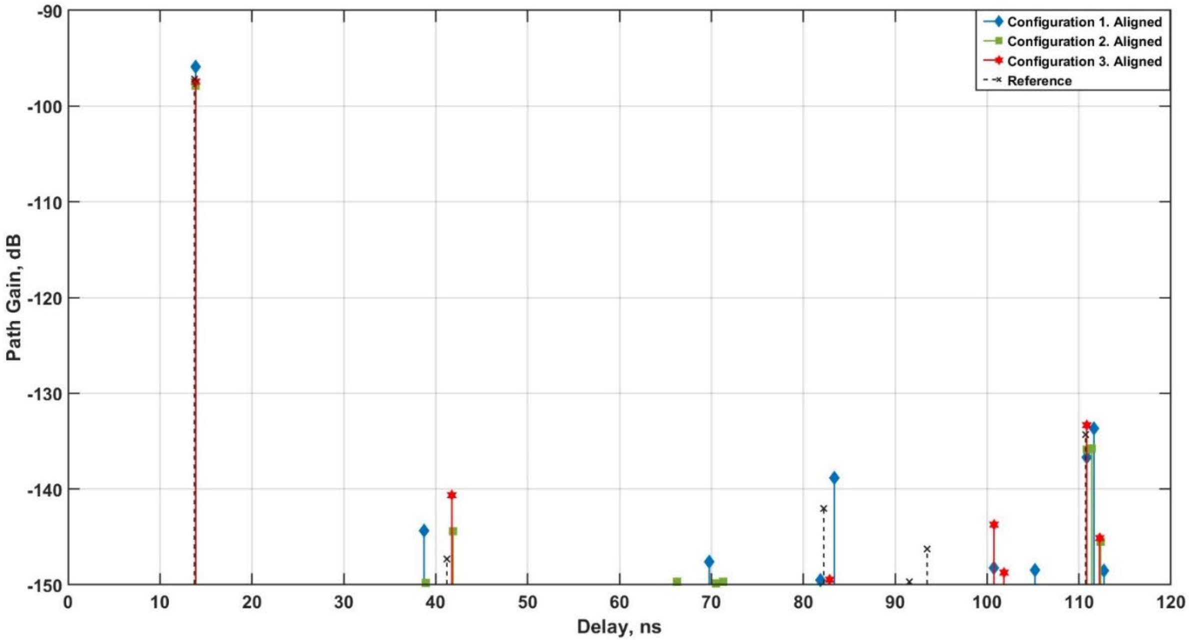

Figure 37 PDP for h_{TX}=1.3m and h_{RX}=1.08m and aligned Tx and Rx (±3°), for three different robotic arm configurations (Setups 5, 7 and 9). The reference measurement is without the robotic arm

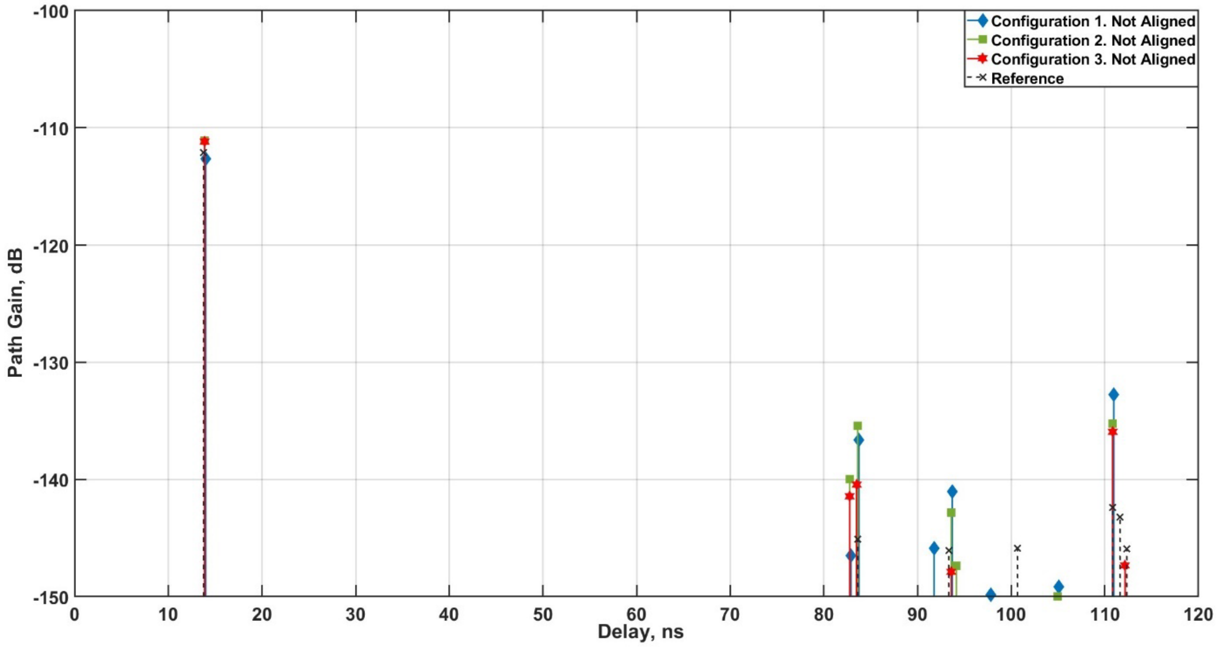

Figure 38 PDP for h_{TX}=1.6m and h_{RX}=1.08m and not aligned Tx and Rx, for three different robotic arm configurations (Setups 10, 12 and 14). The reference measurement is without the robotic arm

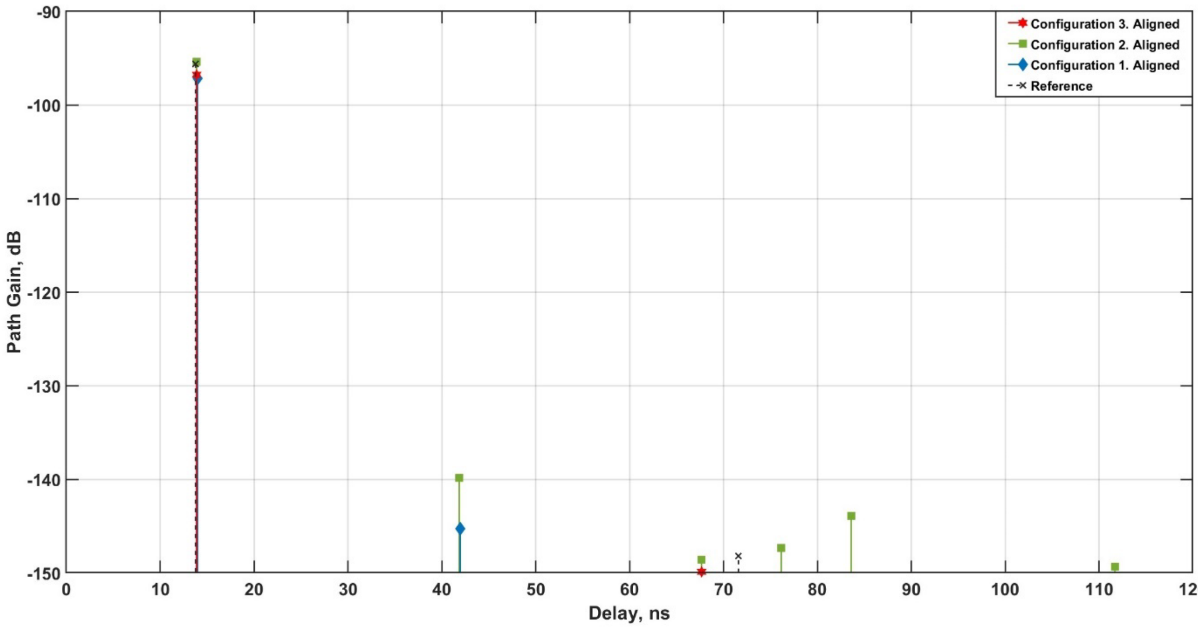

Figure 39 PDP for h_{TX}=1.6m and h_{RX}=1.08m and aligned Tx and Rx (±7°), for three different robotic arm configurations (Setups 5, 7 and 9). The reference measurement is without the robotic arm

5.2.2. Medium machines: moving objects

5.2.2.1. Milling machine: inter-device – HWDU

In this scenario, the window on the milling machine is moved to different positions with 1cm increments, starting with completely closed (Figure 40(a)) to fully open (Figure 40(b)). Therefore, the transmission loss through glass can be measured. In Figure 40(a), while there is a clear LOS, the glass is between the Tx and Rx. In other positions, the window frame is obstructing the LOS (e.g., Figure 40(c)). Later, there is a clear LOS and no glass in between the TX and RX, as shown in Figure 40(d). The RX power of the LOS component for the different opening gaps of the machine's window is displayed in Figure 41. Very small losses by transmission through the glass can be observed in both co-polarized channels. However, there is a loss of approx. 15 dB when the frame is obstructing the LOS.

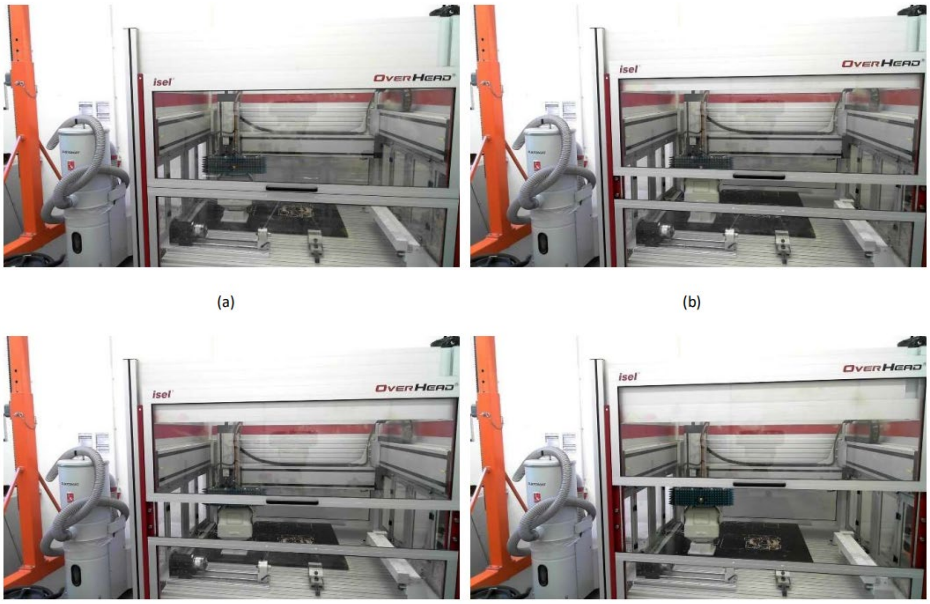

(a) (b)

(c) (d)

Figure 40 Measurement set-up for transmission loss for different positions of the window

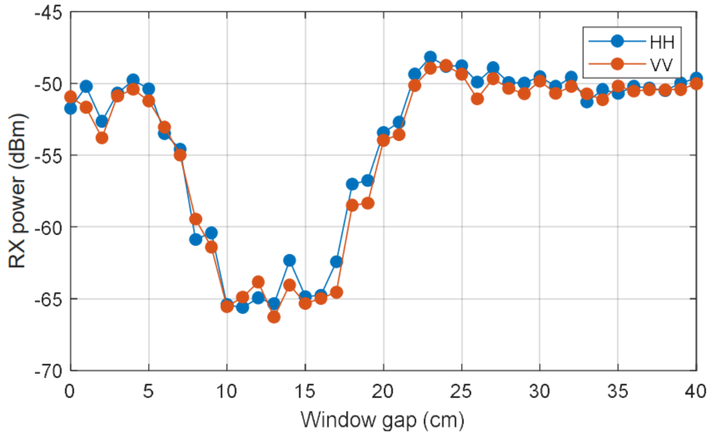

Figure 41 RX power for different opening gaps of the machine's window.

5.2.2.2. Robotic arms: two arms communication with moving obstacle – TUBS

For this inter-device scenario, two robotic arms are placed on opposite sides of a working bench in the robotics lab. A third robotic arm was placed in the middle of them as a moving object (Figure 42). Two different arm movements were performed: a vertical and a rotational movement. The height of the transmitter was varied from 0.98 m up to 1.65 m. The Rx and Tx were aligned only for the lowest position. In total, 6 different setups were measured.

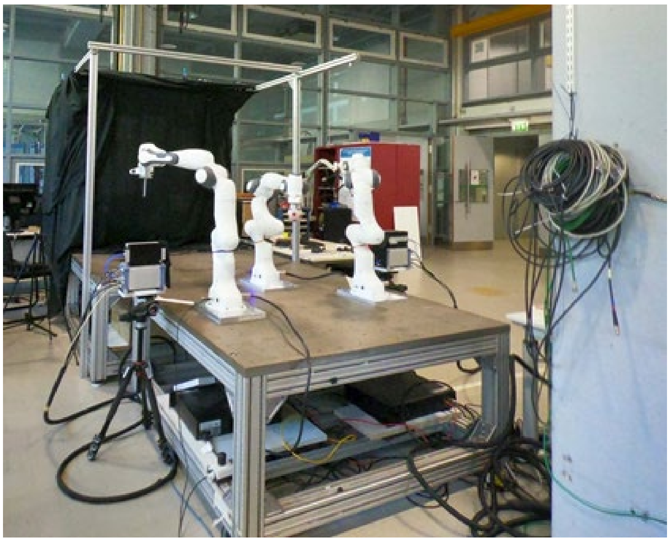

Figure 42 Setup inter-device communication with moving object

For the vertical movement of the arm, we can identify a blockage of the LOS. In Figure 43 the strongest path gain can be seen if Tx and Rx are aligned at a height of 0.98 m. The vertical movement of the moving object is causing a blockage that leads to a drop of the path gain. At the end position (Figure 44(d)), there is still an OLOS that cause a loss of around 15 dB. The maximum blockage can be seen when the object is in position Figure 44(c). In position Figure 44 (a) and b), the moving object has no effect on the channel.

For Tx height = 1.39 m, only a maximum path gain of around -125 dB is received. This is due to the misalignment of Tx and Rx. However, a drop of the gain caused by the movement of the object in between at the position seen in Figure 43. can be identified. For the highest position of 1.65 m, no strong component could be identified. The MPCs are overpowered by the noise.

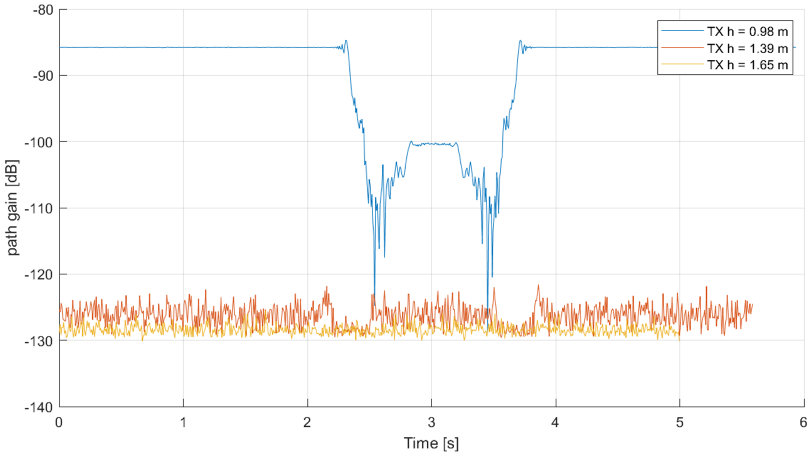

Figure 43 Max Path Gain

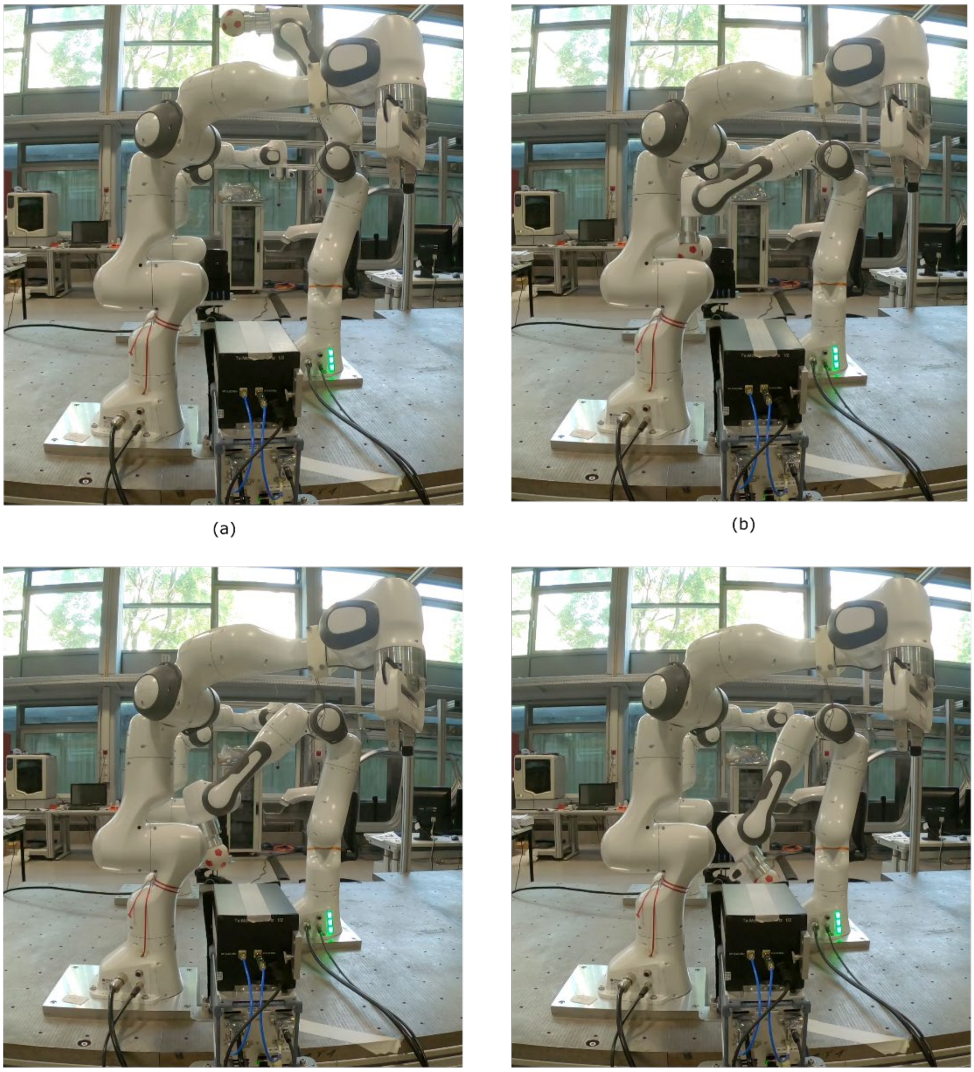

(a)

(b)

(c)

(d)

Figure 44 Vertical movement

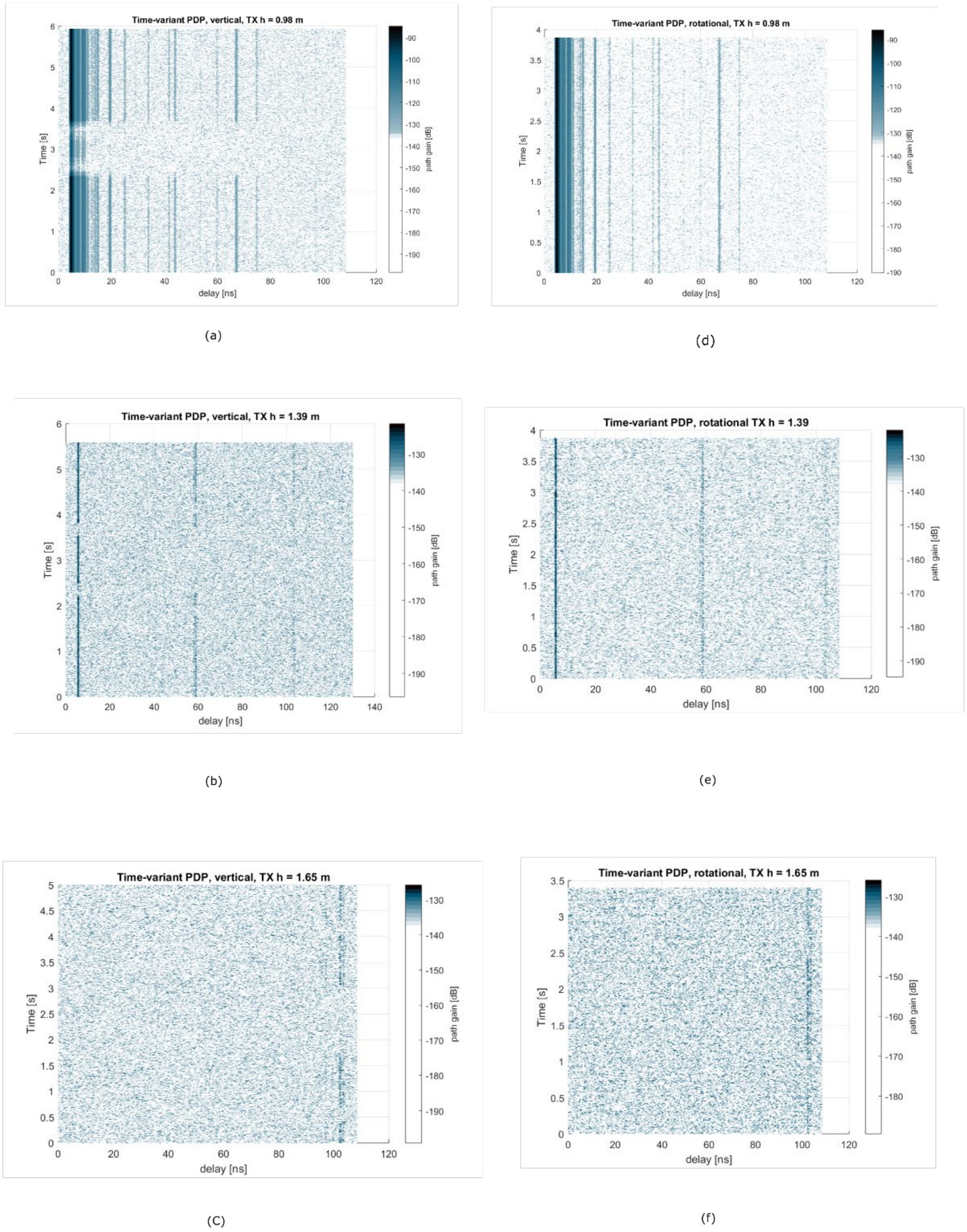

(a) (d)

(b) (e)

(c) (f)

Figure 45 Time-varying PDP for the vertical (a-c) and rotational (d-f) movement

The rotational movement has no strong impact on our communication. When Tx and Rx are at h = 0.98 m, the moving robotic arm is not blocking the LOS and no difference in the path gain can be observed.

We can observe two stronger MPCs around 60 ns and 100 ns for the Tx height of 1.39 and 1.65 (Figure 45 (b-c, e-f)). These are MPCs coming from the environment, as they can also be identified in the reference measurements without any robotic arms placed on the workbench.

5.2.3. Medium machines: moving Tx or Rx

5.2.3.1. Big industrial workspace: access point with moving Rx – TUBS

This scenario represents a THz transmission between an access point and a sensor on a moving machine in the big industrial workspace.

5.2.3.1.1. Experimental Setup

The setup was constructed as follows: the Tx node is fixed on the tripod and located on the upper level of the industrial space. The Rx unit is fixed on the tripod placed on a rail system and located on the lower level of the workspace in the passage between two machine rows. A schematic view is presented in Figure 46 whereas measurement setup photos are provided in Figure 47

The setup parameters are presented in Table 12 and consist in the following data: Tx and Rx heights (h_{Tx}, h_{Rx}); distance between Tx and Wall 1 ($d_{Tx\text{-}W1}$); distance between Rx and Wall 1 ($d_{Rx\text{-}W1}$); distance between Rx and Wall 2 in start point ($d_{Rx\text{-}W2\text{-}start}$); distance between Rx and Wall 2 in the stop point ($d_{Rx\text{-}W2\text{-}stop}$); α_{TX} and α_{RX} are the Tx and Rx elevation angles.

Rx was moved from the start point to the end point (Figure 47 (b)). There were two setups: 1) Tx antenna was aligned, and Rx antenna was not aligned; 2) Tx and Rx antennas were aligned. Movements were performed in the following way: the cable was attached to the base of the rails platform and then it was pulled. For each setup, 4 moving measurements were performed. Since the cable was manually pulled “by hands”, the speed was slightly different across the measurement although the mean speed value was 0.33 m/s.

5.2.3.1.2. Measurement evaluation and results

The time-varying channels were measured to obtain 3D CIR matrices (Power x Time x Delay). Each 3D matrix was calibrated in terms of path gain and delay using a B2B measurement performed before the measurements. The 3D PDP were created based on these calibration matrices.

The 3D PDPs for aligned and non-aligned cases are presented in Figure 48.

Maximum peaks were observed with delays around 27 ns. For this delay value, 2D plots (Power x Distance) were created to compare the aligned with the non-aligned cases (Figure 49).

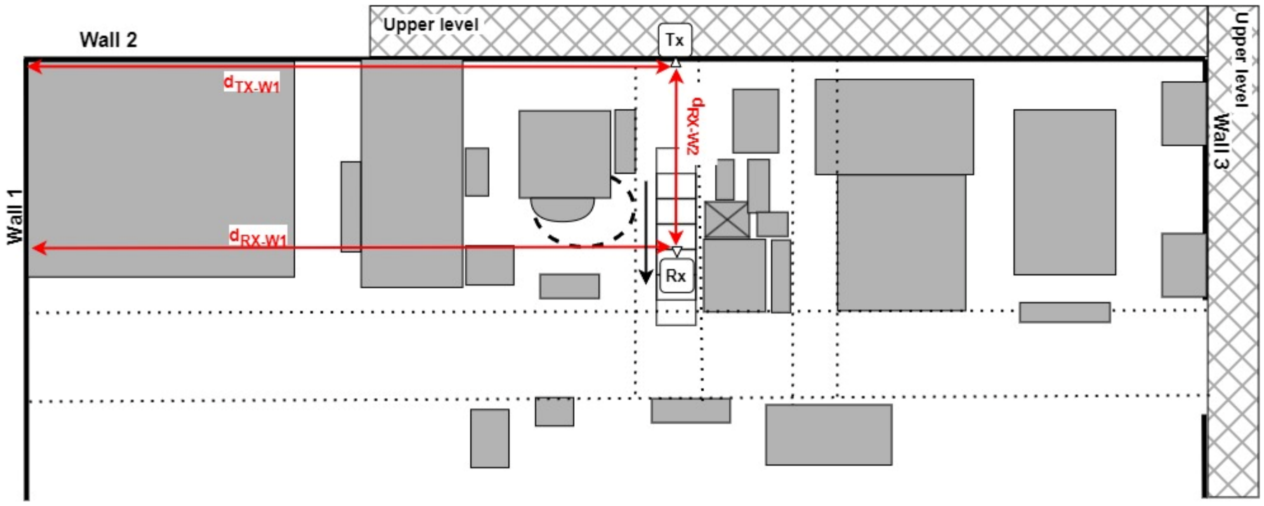

Figure 46 schematic top view of the “Access point” with moving Rx

Table 12 Setup parameters

Setup number	h_{Tx}, m	h_{Rx}, m	$d_{Tx\text{-}W1}$, m	$d_{Rx\text{-}W1}$, m	$d_{Rx\text{-}W2\text{-}START}$, m	$d_{Rx\text{-}W2\text{-}STOP}$, m	α_{Tx}°	α_{Rx}°
1	5.26	1.25	20.7	20.7	5.1	7.3	-35	0
2	5.26	1.25	20.7	20.7	5.1	7.3	-35	35

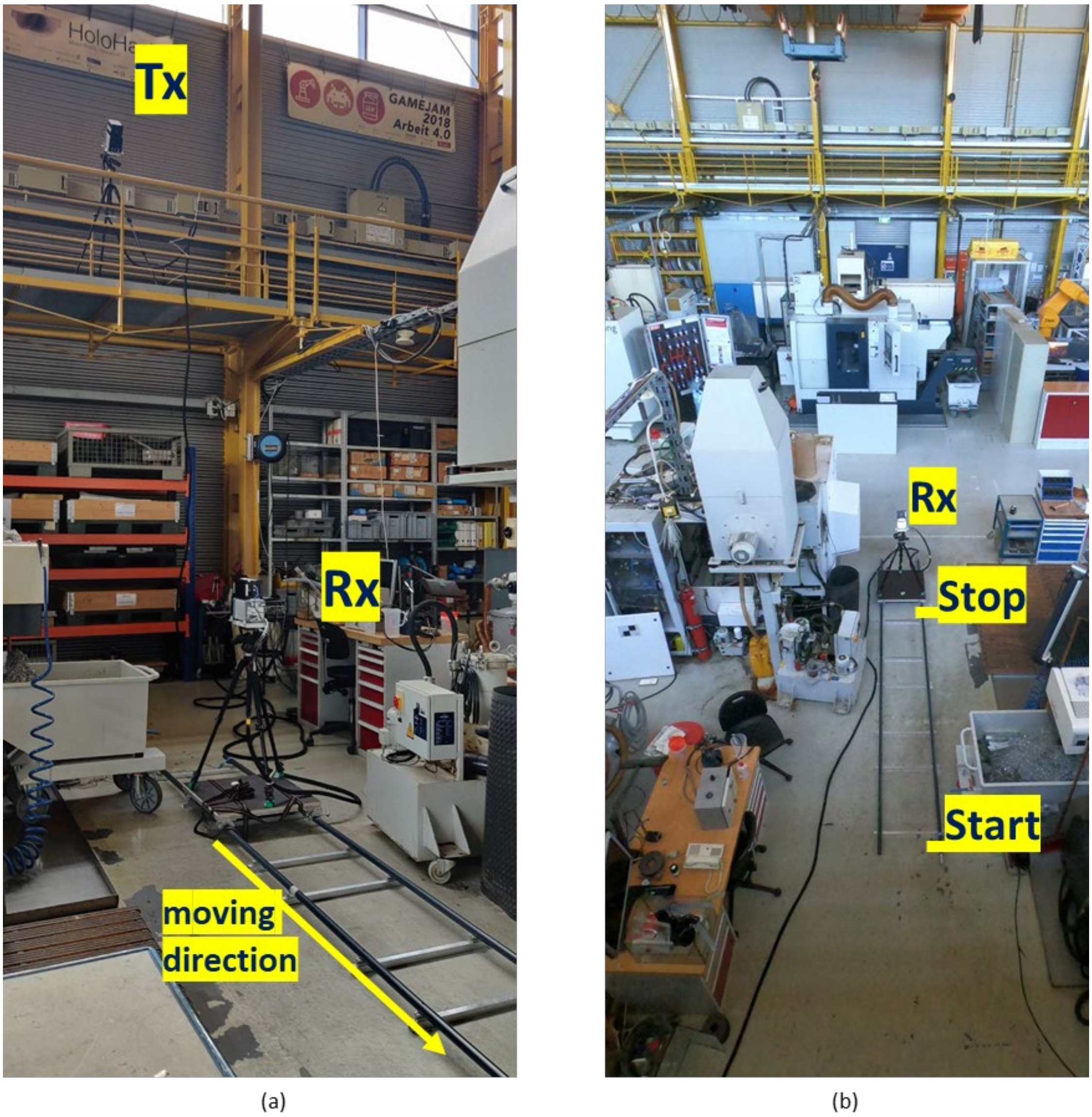

(a) (b)

Figure 47 Measurement setup photos

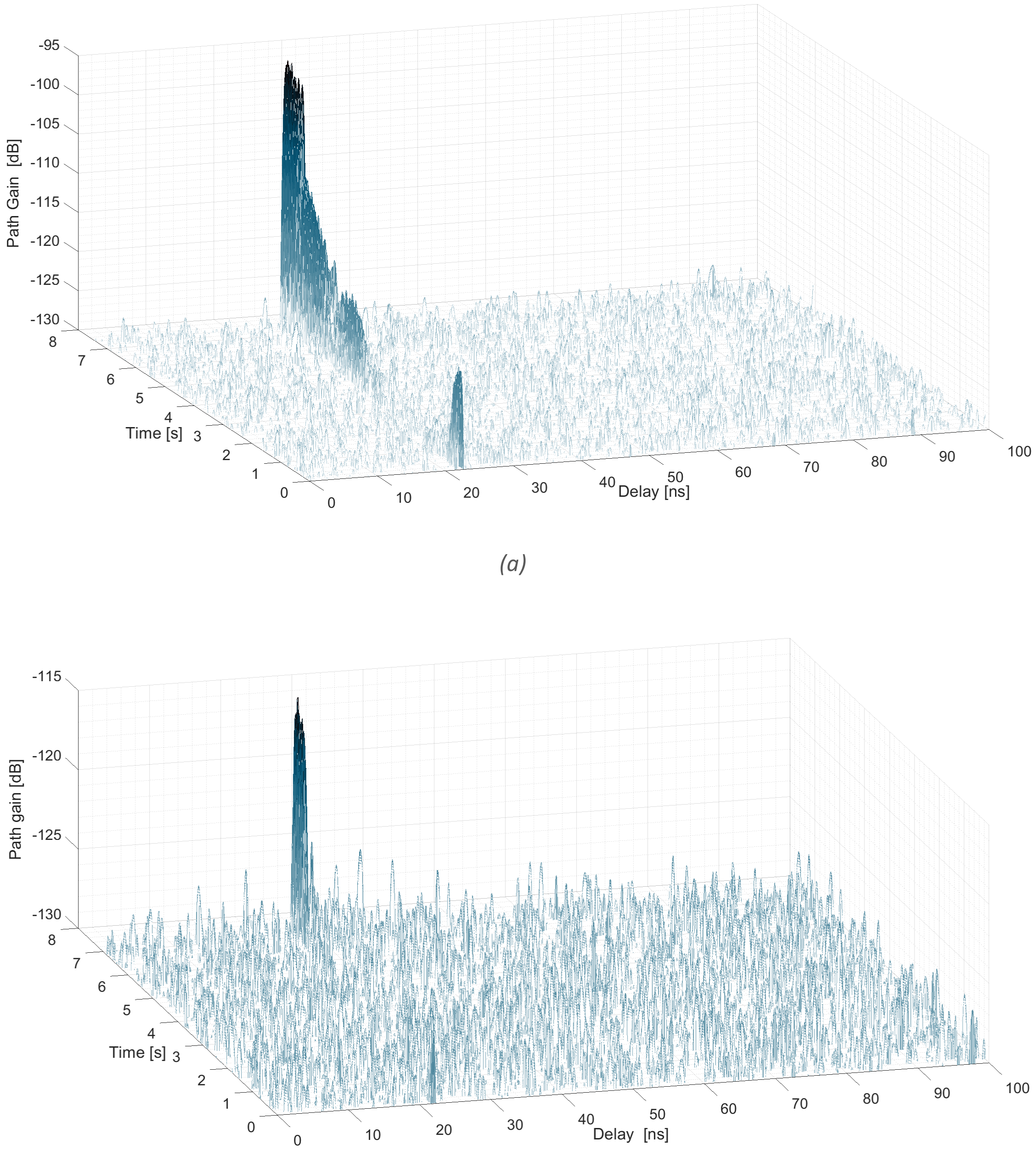

(a)

(b)

Figure 48 Time-varying PDP when Rx is (a) aligned Rx, and (b) misaligned

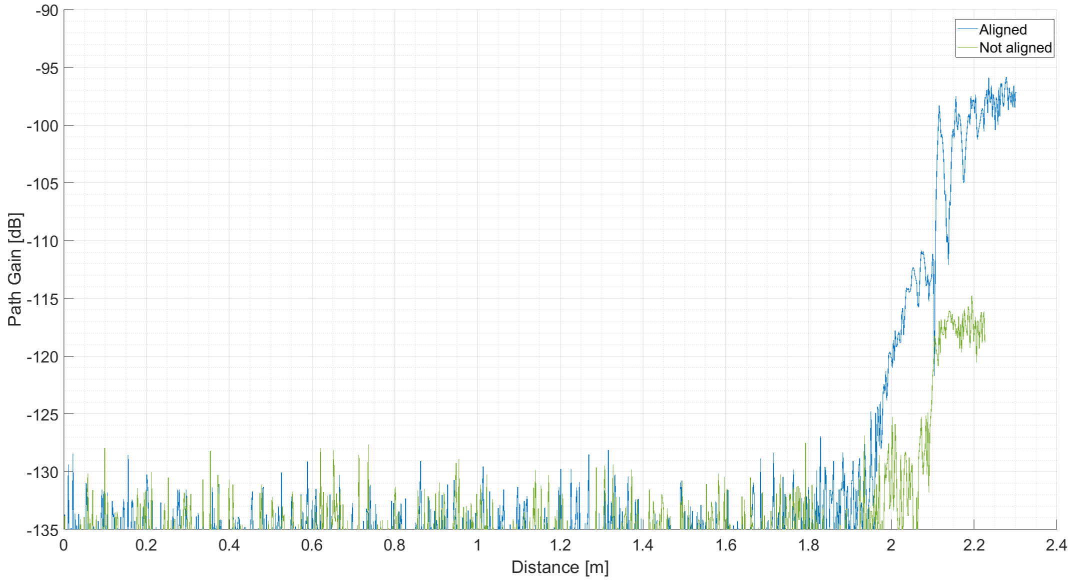

Figure 49 Path Attenuation versus distance for aligned and not aligned setups

5.3. Intra-device scenarios

5.3.1. Medium machine: static condition

5.3.1.1. Milling machine: intra-device – HWDU

This intra-device scenario represents a THz transmission between two sensors inside of a machine. For this case, both Rx & Tx are inside the milling machine depicted in Figure 50 wherein the distance between them is ranging between 50 cm - 140 cm. The environment configuration is shown in Table 13.

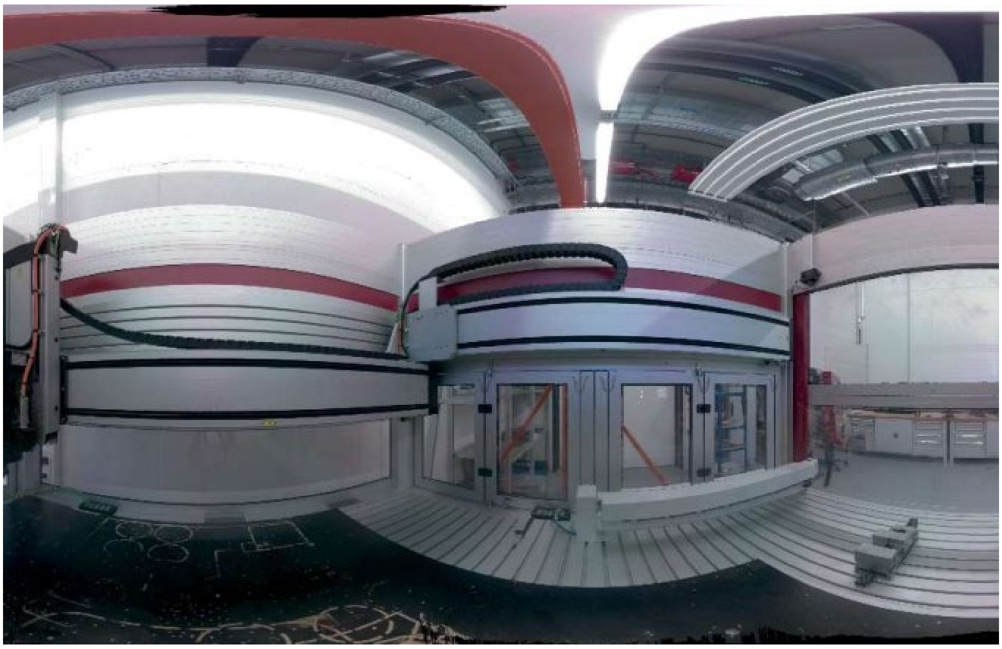

Figure 50 Environment inside the milling machine for intra-device scenario

The same link with the axes and milling head in a fixed position was measured with 5° HPBW antennas at the Rx and open wave guide (OWG) at the Tx. The results displayed in Figure 51 show the specific interaction points of the angles of arrival corresponding to the specular reflections. These specular interaction points are very sparse. Apart from the LOS component, only reflections from the positioners of the milling head and frames of the machine can be observed. In addition, there are reflections from other machine components as the holders in the lower part in the azimuth range of -120° to 135° and elevation -15° to -45°. Reflections in this structure are stronger in the vertical polarization, as shown in Figure 52.

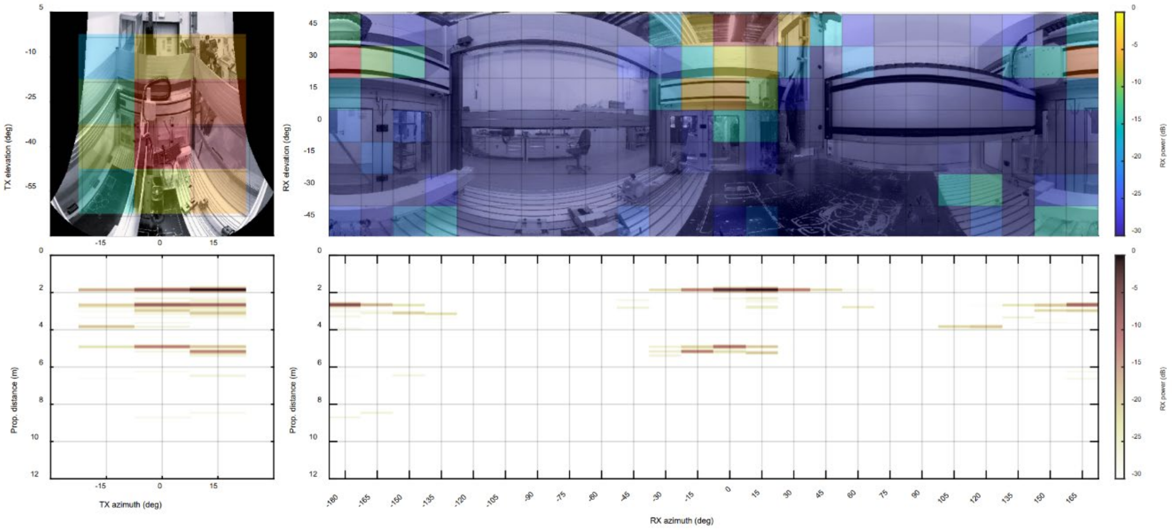

Figure 51 PAEP and PADP for the LOS

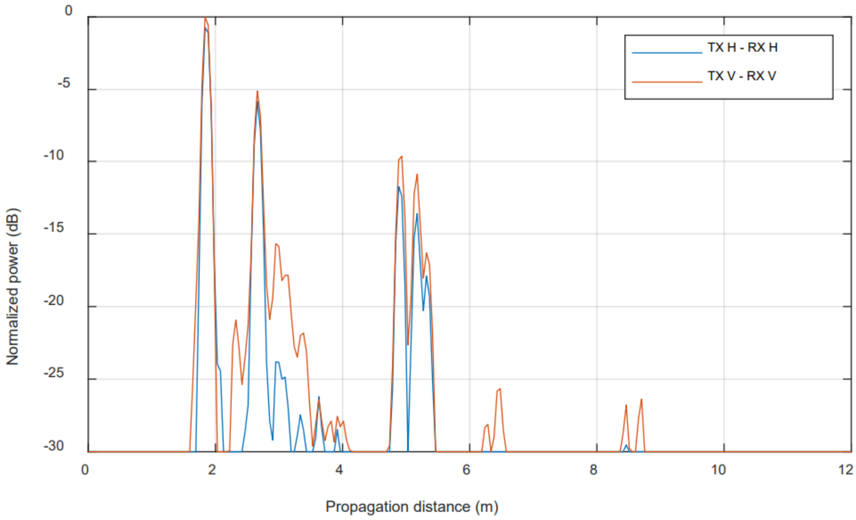

Figure 52 polarimetric PDP for the LOS

Table 13 summarizes the channel parameters extracted from measurements for the different investigated configurations.

Table 13 List of parameters from measurements

Configuration	Visibility	Gain[1] (dB)	DS[2] (ns)	ASA (°)	ESA (°)	ASD (°)	ESD (°)
Axes of the milling head close to the RX, milling head on the left side of the RX	LOS 1	-80.67	3.23	75.16	18.41	8.76	11.68
Axes of the milling head in the middle of the machine, milling head in the middle	LOS 2	-82.19	2.91	74.58	19.03	9.13	10.17

Axes of the milling head in the rear of the machine, milling head in the left side	LOS 3	-80.57	3.41	71.73	17.56	8.75	11.75

[1] Isotropic channel gain: averaged over Tx angular scans and summed over Rx angular scans

[2] Calculated with 20 dB dynamic range

6. EMF exposure aspects of THz

Controlling and reducing EMF exposure are among the targets for the SNS work programme. These can be summarized to cover *safety, awareness, control,* and *reduction*. This can be done e.g., by means of advanced antenna systems to control the exposure level. The 5G-PPP TMV Working Group has published a white paper discussing EMF for 6G [4]. This document also gives a good overview of the possible challenges.

Guidelines and exposure limits are developed by the International Commission on Non-Ionizing Radiation (ICNIRP)[1], which is an independent NGO with experts in the field. These guidelines are endorsed by the World Health Organization (WHO) and adopted as regulation in most European countries. Some countries are enforcing more restrictive rules. The "ICNIRP Guidelines for Limiting Exposure to Electromagnetic Fields (100 kHz to 300 GHz)" [5] was revised in 2020 based on new evidence of the potential health risks. As reflected in the title, these guidelines cover frequencies up to 300 GHz, and TIMES might be interested in the range up to 1 THz. Similar guidelines above 300 GHz do not exist, however, the frequency range is covered by guidelines on limits of exposure to incoherent visible and infrared radiation [6], however, exposure due to communication signals is not included here. Thus, for the moment we can only take the frequency range up to 300 GHz into account.

The ICNIRP RF guidelines cover exposure both from devices in terms of Specific Absorption Rate (SAR), and electric/magnetic field (E/H) exposure measured as field strength (V/m, A/m) and power density (W/m^2). They are based on the whole body and local temperature rise and can be distinguished between «Occupational» and «General public» exposure (factor 5:1). Different averages are given (6 minutes and 30 minutes). For the higher frequencies of the whole body, the occupational exposure limit (6-minute average) is defined as 50 W/m^2, while for the public, the limit value is 10W/m^2. Figure 53 shows the E/H field and power density limits for public exposure over the whole range of 100 kHz-300 GHz.

---

[1] https://www.icnirp.org/

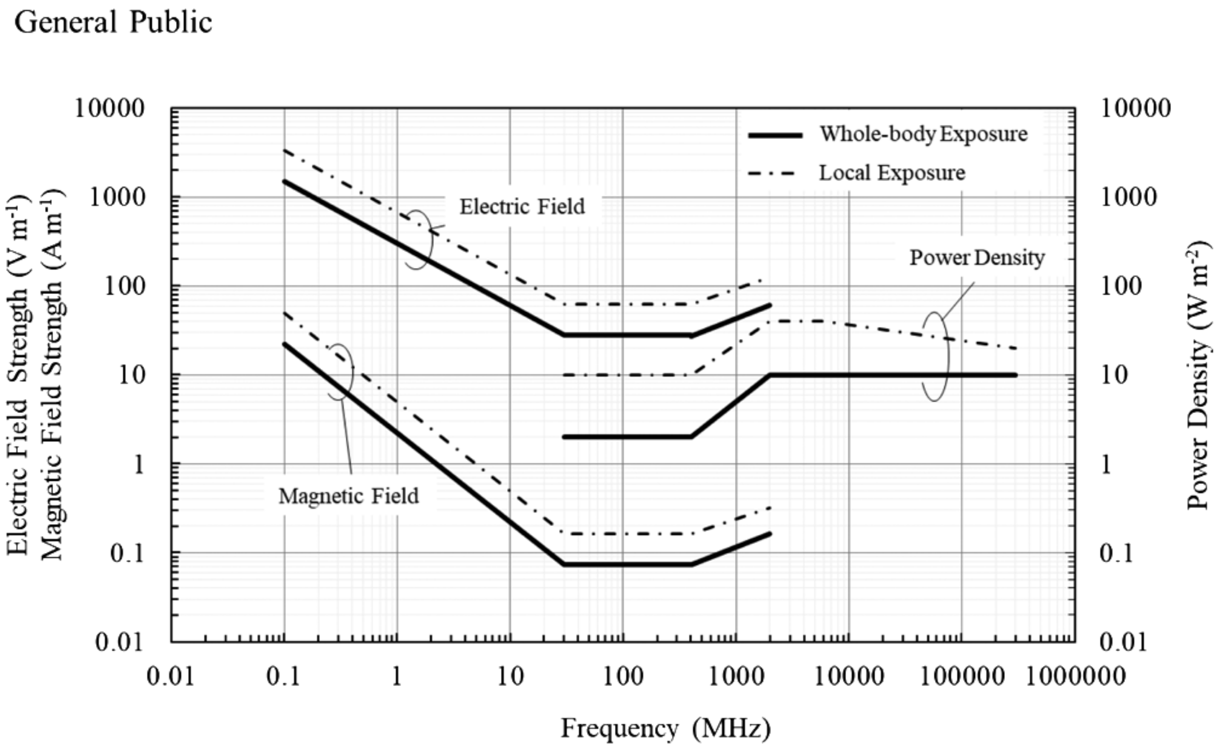

Figure 53 Reference levels for time averaged general public exposures of ≥6 min, to electromagnetic fields from 100 kHz to 300 GHz (source: ICNIRP [5]).

In order to control and assess that exposure limits are conformed with; standardized measurement methods are needed. Such methods are mainly developed by the International Electrical Committee (IEC) Technical Committee and the ITU. IEC (TC) 106 “Methods for the assessment of electric, magnetic and electromagnetic fields associated with human exposure”, has the scope to prepare international standards on measurement and calculation methods to assess human exposure to electric, magnetic and electromagnetic fields[2] [7] [8]. ITU-T Study Group 5 (SG5)[3] is the lead study group on ICT environmental aspects of electromagnetic phenomena and climate change, where Question 7/5: “Human exposure to electromagnetic fields (EMFs) due to radio systems and mobile equipment” covers the work. EMF assessment is covered mainly by the ITU-T K-series of recommendations for EMF assessment[4]. The ITU-R has also published a report on EMF in the Spectrum Management (SM) series [9].

Following this introduction, the TIMES approach for analysing EMF in a THz scenario will be to revisit the ICNIRP guidelines in more detail, and the measurement methods from the IEC and ITU, and other relevant sources. Furthermore, an analysis of the potential exposure covering some of the TIMES scenarios and use cases will be done, possibly by analysing the channel measurements on pathloss and coverage. This will be further covered in later TIMES deliverables D3.2 and D3.4.

---

[2] https://www.iec.ch/dyn/www/f?p=103:7:0::::FSP_ORG_ID,FSP_LANG_ID:1303,25

[3] http://www.itu.int/en/ITU-T/emf/Pages/default.aspx

[4] https://www.itu.int/net/ITU-T/lists/standards.aspx?Group=5&Domain=40

7. Conclusions

This deliverable provides a detailed report of channel measurements taken at 300 GHz in industrial environments. It includes an overview of the used workspaces and equipment, a detailed description of the measurement setups and recent measurement data analysis. Measurements include inter- and intra-device as well as static and dynamic scenarios and characterization of PL and LSPs in different visibility conditions.

Characterization of PL and LSPs in an industrial workshop environment was conducted across three frequency bands (sub-6 GHz, mmWave, and THz), yielding the following results:

- LSPs comparison across different frequency bands revealed no clear correlation between DS, ASA, ASD, and frequency band. However, average values tend to be larger at higher frequencies.
- The ABG model was parametrized based on the measurements and compared with Close-In, 3GPP and ITU models as well as with PL measurement values. It was observed that the 3GPP TR 38.901 model better fits the measurements in comparison to the ITU-R P.1238-11 model, especially for NLOS cases.

Analysis of static inter-device scenarios provided the following observations:

- For the OLOS case, the strongest component can either be the LOS component, such as in the large industrial workspace "Access Point," or a reflection path, as seen in the static inter-device "Milling Machine" scenario. However, in both scenarios, the OLOS path exhibited a lower signal strength than the unobstructed path. The difference is approximately 16 dB in the "Access Point" scenario and approximately 4 dB in the inter-device "Milling Machine" scenario.
- Communication is still possible in the case of a NLOS scenario. For example, in the big industrial workspace “Access Point” scenario, the strongest component was -141.7 dB for NLOS and -117.4 dB for LOS.

In addition to the static measurements, three dynamic scenarios were conducted: two involving a moving obstacle and one with a moving Rx.

- In the first moving obstacle scenario, the milling machine window moved to different positions: from completely closed to fully open. In between, the window frame partly obstructed the LOS path, resulting in a signal loss of approximately 15 dB.
- The second moving obstacle scenario was realized using the robotic manipulator. Moving arm generated a blocking effect resulting in an OLOS path between Tx and Rx with a characteristic signal reduction of approximately 15 dB in the strongest component.
- The scenario with moving Rx included options with partly aligned and misaligned Tx and Rx antennas and demonstrated that communication was possible only on some sections of the moving track.

The intra-device scenario, conducted inside the milling machine, revealed that apart from the LOS component, there were only a few reflection components originating from the positioners of the milling head and the frames of the machine. Additionally, it was observed that these reflections within the structure are stronger in the vertical polarization.

In general, the observations in the THz range highly reflective industrial environments, characterized by the high density of machines and metal surfaces, indicated that wireless communication is feasible not only in the LOS scenarios but also in the OLOS and NLOS setups, owing to the presence of MPCs. However, this fact highlights the need for further research on delay and angular spread in such environments.

Finally, the presented data and results are intended to serve as a fundamental baseline for the development of channel models.

References

[1] A. Schultze, M. Schmieder, S. Wittig, H. Klessig, M. Peter, W. Keusgen, “Angle-Resolved THz Channel Measurements at 300 GHz in an Industrial Environment,” in *IEEE 95th Vehicular Technology Conference*, Helsinki, 2022.

[2] D. Dupleich, A. Ebert, Y. Völker-Schöneberg, L. Löser, M. Boban, and R. Thomä, “Spatial/Temporal Characterization of Propagation and Blockage from Measurements at sub-THz in Industrial Machines,” in *17th European Conference on Antennas and Propagation (EuCAP)*, Florence, 2023.

[3] S. Rey, J. M. Eckhardt, B. Peng, K. Guan and T. Kürner, “Channel sounding techniques for applications in THz communications: A first correlation based channel sounder for ultra-wideband dynamic channel measurements at 300 GHz,” in *9th International Congress of Ultra Modern Telecommunications and Control Systems and Workshops (ICUMT)*, Munich, 2017.

[4] 5G PPP Whitepaper, “Beyond 5G/6G EMF Considerations». 5G PPP TMV WG/EMF TF, July 2023. DOI 10.5281/zenodo.8099834.,” [Online]. Available: https://zenodo.org/record/8099834.

[5] ICNIRP guidelines for limiting exposure to electromagnetic fields (100 kHz to 300 GHz), “In: Health Phys 118(5): 483-524,” 2020. [Online]. Available: https://www.icnirp.org/cms/upload/publications/ICNIRPrfgdl2020.pdf .

[6] ICNIRP Guidelines on limits of exposure to incoherent visible and infrared radiation, “Health Phys 105(1):74-96,” 2013. [Online]. Available: https://www.icnirp.org/cms/upload/publications/ICNIRPVisible_Infrared2013.pdf .

[7] IEC/TR 63232:2017, “Determination of RF field strength, power density and SAR in the vicinity of radiocommunication base stations for the purpose of evaluating human exposure”.

[8] IEC/TR 62669:2019, “Case studies supporting IEC 62232 - Determination of RF field strength, power density and SAR in the vicinity of radiocommunication base stations for the purpose of evaluating human exposure”.

[9] ITU-R Report SM.2452-1, “Electromagnetic field measurements to assess human exposure,” 07 2022. [Online]. Available: https://www.itu.int/pub/R-REP-SM.2452 .

[10] IEC/TR 62669:2019, “Case studies supporting IEC 62232 - Determination of RF field strength, power density and SAR in the vicinity of radiocommunication base stations for the purpose of evaluating human exposure”.

[11] ITU-R Report SM.2452-1, “Electromagnetic field measurements to assess human exposure,” 07 2022. [Online]. Available: https://www.itu.int/pub/R-REP-SM.2452 .